JCI insight

Proteomics-based evaluation of AAV dystrophin gene therapy outcomes in mdx skeletal muscle

Erynn E. Johnson, Theodore R. Reyes, Jeffrey S. Chamberlain, James M. Ervasti, Hichem Tasfaout

JCI Insight. 2025. https://doi.org/10.1172/jci.insight.197759.

Research In-Press Preview Genetics Muscle biology

Graphical abstract

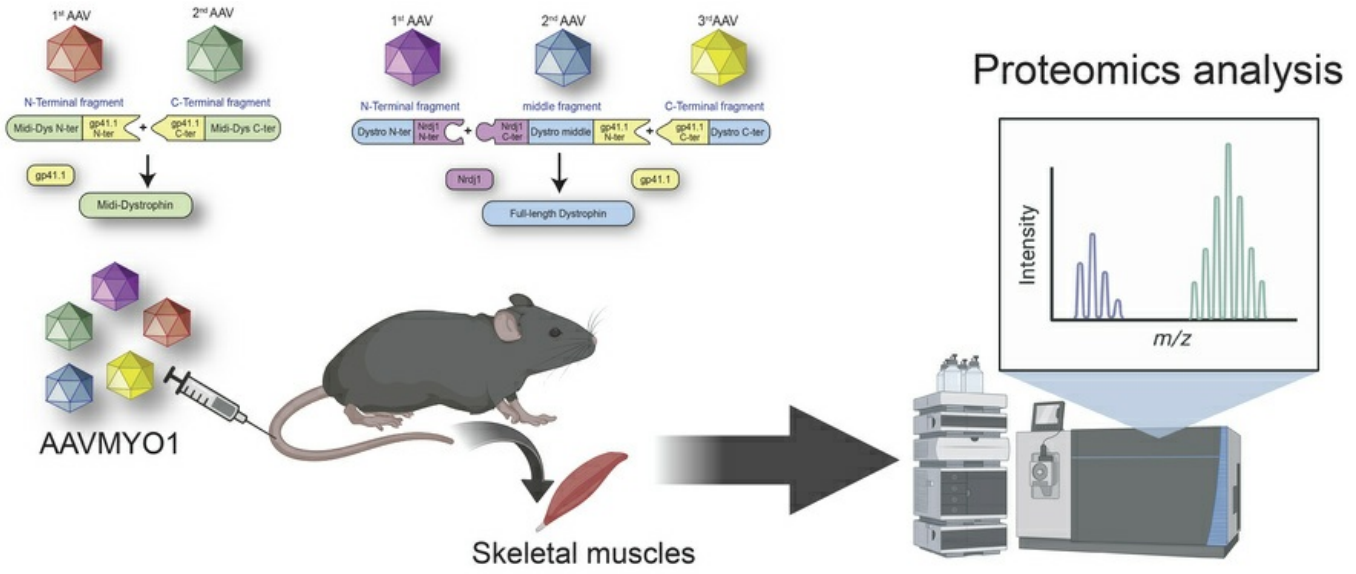

Find the latest version:

https://jci.me/197759/pdf

Proteomics-based evaluation of AAV dystrophin gene therapy outcomes in mdx skeletal muscle

Erynn E. Johnson[1], Theodore R. Reyes[2,3], Jeffrey S. Chamberlain[2,3,4], James M. Ervasti[1], Hichem Tasfaout[2,3*]

[1]Department of Biochemistry, Molecular Biology and Biophysics, University of Minnesota - Twin Cities; Minneapolis, MN.

[2]Department of Neurology, University of Washington School of Medicine; Seattle, Washington, USA.

[3]Senator Paul D. Wellstone Muscular Dystrophy Specialized Research Center, University of Washington School of Medicine; Seattle, Washington, USA.

[4]Department of Biochemistry, University of Washington School of Medicine; Seattle, Washington, USA.

Correspondence to: Dr. Hichem Tasfaout, Department of Neurology, University of Washington School of Medicine, Seattle, Washington, USA.

Phone: +1.206.221.5412

E-mail: tasfaout@uw.edu

Conflicts of interest

H.T. and J.S.C. are inventors of a patent describing the use of the split intein technology to express large proteins in muscular disorders, which was licensed by KineaBio. H.T and J.S.C serve as scientific advisors to KineaBio. The other authors declared no competing interests.

Abstract:

Duchenne muscular dystrophy (DMD) is a fatal genetic muscle-wasting disease characterized by loss of dystrophin protein. Therapeutic attempts to restore a functional copy of dystrophin to striated muscle are under active development, and many utilize adeno-associated viral (AAV) vectors. However, the limited cargo capacity of AAVs precludes delivery of full-length dystrophin, a 427 kDa protein, to target tissues. Recently, we developed a method to express large dystrophin constructs using the protein *trans*-splicing (PTS) mechanism mediated by split inteins and myotropic AAV vectors. The efficacy of this approach to restore muscle function in *mdx*^{4cv} mice was previously assessed using histology, dystrophin immunolabeling, and western blotting. Here, we expand our molecular characterization of dystrophin constructs with variable lengths using a mass spectrometry-based proteomics approach, providing insight into unique protein expression profiles in skeletal muscles of wild-type, dystrophic *mdx*^{4cv}, and AAV-treated *mdx*^{4cv}. Our data reveal several affected cellular processes in *mdx*^{4cv} skeletal muscles with changes in the expression profiles of key proteins to muscle homeostasis, whereas successful expression of dystrophin constructs results in an intermediate to complete restoration. This study highlights several biomarkers that could be used in future preclinical or clinical studies to evaluate the effectiveness of therapeutic strategies.

Introduction

Duchenne muscular dystrophy (DMD) is an inherited, lethal X-linked muscle-wasting disease. Affected patients typically show the first symptoms at ~ 3 years of age (1). The muscle function deteriorates rapidly starting at the age of 7 years with pronounced muscle weakness, chronic inflammation, and fibrosis, leading to loss of ambulation and premature death in the second to the third decade of life due to cardiorespiratory complications. DMD is caused by loss-of-function mutations in the *DMD* gene that abolish the production of a functional dystrophin (2-4). In muscle, dystrophin constitutes a key partner to several proteins, which together form the dystrophin-glycoprotein complex (DGC) (5). This complex plays an important role in preserving myofiber integrity during muscle contraction by connecting the intracellular cytoskeleton to the extracellular matrix and serves as a molecular anchor to proteins involved in cellular signaling pathways regulating myofiber homeostasis (6).

Since DMD is a monogenic disease, restoring muscle function by supplying a functional copy of a dystrophin gene is a highly appealing therapeutic strategy. Several preclinical and clinical programs are in development to evaluate the efficacy and safety of systemic delivery of adeno-associated viral (AAV) vectors carrying dystrophin-based constructs to striated muscles (7). These vectors have been successfully used to express transgenes in a variety of organs, such as the liver, brain, retina, and muscles, and have shown a robust and long-term expression of transgenes with superior efficacy compared to other viral or non-viral vectors. However, AAV particles are relatively small (~20 nm) and, thus, present a limited packaging capacity to sequences of less than 5 kb (8), which poses an enormous challenge to genetic disorders with larger proteins like DMD. Dystrophin muscle isoform (Dp427) is expressed from an 11.2 kb cDNA, which far exceeds the AAV maximal packaging capacity.

Therefore, tremendous efforts have been made over the last decades to study the structural organization of dystrophin, which later led to the development of a new class of dystrophin-based gene therapies. Early studies have shown that large in-frame deletions (up to 46%) within the central rod domain result in the production of a mini-dystrophin that retains functionality and protects striated muscle from mechanical damage (9). Additional phenotypical characterizations of transgenic mice demonstrate the efficacy of these mid-size dystrophins and shed light on the modular organization of dystrophin (10-12). These studies also showed that truncated dystrophins, termed micro-dystrophins (μDys), that fit within the AAV cargo capacity are stable and functional. The administration of AAV-μDys vectors into DMD animal models resulted in significant correction of muscular dystrophy (13-16). Several μDys constructs are being evaluated in the clinic, with one drug already approved by the FDA (Elevidys®). Nonetheless, an increasing number of preclinical and clinical data point to incomplete muscle recovery with various μDys constructs. This suggests the need to express larger dystrophins to fully restore the functional impairment.

Recently, we described a method for delivering and expressing large dystrophins using protein *trans*-splicing (PTS) mediated by split inteins and myotropic AAV vectors (17). PTS is a natural phenomenon originally discovered in unicellular organisms by which two protein halves are seamlessly fused into a functional protein (18). We adapted this post-transcriptional process to express a large midi-dystrophin (midi-Dys ΔSR5-15) or full-length dystrophin (Dp427 isoform) using, respectively, a dual or triple AAV approach (17, 19). With this method, efficient reconstitution of large dystrophin was achieved using low doses of the AAVMYO1 (2-4 10^{13} vg/kg) in both young (mildly affected) or old (severely affected) *mdx*^{4cv} mice, which restored several functional defects to normal levels. Nonetheless, the molecular characterization of the

phenotypical rescue was limited to histology assessment using common staining methods, immunolabeling of dystrophin and its glycoprotein partners, or western blotting. Although valuable to determine the protein expression and distribution, as well as the general muscle morphology, alternative methods that give deeper insight into specific defects or protein regulation may identify biomarkers that better delineate the stages of disease progression and serve as outcome measures in clinical trials conducted using AAV-dystrophin approaches.

Here, we describe a sensitive mass spectrometry-based proteomics workflow that allows a holistic analysis of protein expression of wild-type, saline- or AAV-treated *mdx*^{4cv} mice. Our data revealed subtle changes in dystrophic muscles expressing different dystrophin-based constructs and led to the identification of cellular biomarkers with variable expression profiles.

Results

Validation of dystrophin gene therapy replacement

We employed an isobaric labeling multiplex discovery proteomics approach to compare the skeletal muscle proteomes of healthy (wild-type, WT), dystrophic (*mdx*^{4cv}), and AAVMYO1-treated *mdx*^{4cv} mice with variable dystrophin constructs. Myotropic AAVMYO1 vectors were administered systemically into 8-week-old mice at low doses of $2x10^{13}$ vg/kg to express µDys5 (ΔSR2-15, Δ18-21, ΔCT) from a single vector or midi-Dys (ΔSR5-15) from dual vector, whereas triple AAVMYO1 were mixed and injected at a total dose of $4x10^{13}$ vg/kg to express full-length dystrophin (Figure 1, A-C). Three months later, gastrocnemius muscles were collected from six AAV-treated mice as well as age-matched saline-treated *mdx*^{4cv} and WT mice. Protein lysates were extracted and labeled with TMT isobaric tags, and two proteomics screens were conducted (Figure 1D).

To verify dystrophin expression in each experimental group, construct-specific dystrophin peptide abundances were assessed (Table 1). Transgenic dystrophin constructs were detected in the samples from *mdx*^{4cv} mice treated with single, dual, or triple AAVs, but at lower abundance *versus* endogenous dystrophin in WT muscles (Figure 2A). As expected, the average abundance of peptide sequences specific to full-length dystrophin was found elevated exclusively in WT or triple-AAV groups (Figure 2B). Similarly, peptide sequences specific to transgenic/human dystrophins (µDys5, intein-generated midi-Dys or full-length dystrophin) were elevated across all AAV treatment groups (Figure 2C). Using different peptides, µDys and midi-Dys were detected at comparable levels, whereas average full-Dys abundance was slightly lower. Finally, by searching peptides specific to large dystrophin (i.e., excluding µDys), we confirmed the exclusive expression of large dystrophins in WT or *mdx*^{4cv} treated with dual or triple AAV vectors (Figure 2D). Overall,

the abundance of the dystrophins was peptide-dependent, with a variable sensitivity observed from one peptide to another.

Together, these data highlight the specificity of this approach to detecting and quantifying endogenous or ectopic dystrophin proteins using specific sequences in healthy or dystrophic muscles post-AAV treatment with different gene replacement approaches.

Muscle histology improvement after dystrophin expression

To evaluate the muscle histology and compare the therapeutic benefits of each gene replacement modality, serial cross-sections of gastrocnemius were stained with Hematoxylin and Eosin (H&E), Trichrome or immunolabeled using specific antibodies raised against elements of the dystrophin-glycoprotein complex or periostin. In the group treated with AAVs, dystrophin expression was detected in 40-60% of myofibers, whereas a few revertant fibers, not exceeding 1%, were found in the saline group (Figure 3A and B). As gastrocnemius muscles are predominantly composed of fast-twitch myofiber type II, more than 86% of dystrophin-positive fibers were either type IIa, IIb, or IIx (Supplementary Figure 1). Muscles from animals treated with saline presented typical dystrophic muscle histology with small fibers and fibrotic and infiltrated muscle tissue compared to WT muscles (Figure 3A, 3C-E). In contrast, muscle from *mdx*^{4cv} mice treated with AAVs showed improved histology with a substantial increase in myofiber area and diameter, with the highest values observed with large dystrophins (i.e., midi- and full-length dystrophin). A marked reduction in collagen content was also found in groups treated with AAVs (Figure 3A, C). Similarly, immunolabeling of periostin showed an increased area in saline-treated dystrophic muscles, confirming the expansion of the extracellular matrix, which AAV-dystrophin treatment prevented (Figure 3F). Interestingly, while proteomics data confirmed the upregulation of periostin (Figure 3G), variable abundance of collagen isoforms was observed. For instance, collagen isoform I

(alpha 1 and 2), IV (alpha 1 and 2), VI (alpha 1, 2, and 3) and XII abundance was unchanged among groups, whereas collagen type III (alpha 1), V (alpha 2 and 3), VI (alpha 6), and XIV (alpha 1 chain) abundance was elevated in *mdx*^{4cv} muscle and restored by AAV treatment (Figure 3H, Supplementary Figure 2).

Characterization of molecular changes using proteomics

Next, we investigated general trends in protein expression profiles between WT, *mdx*^{4cv}, and AAV treatment groups. Dystrophin-deficient *mdx*^{4cv} gastrocnemius muscle displayed a large number of differentially expressed proteins (DEPs) compared to WT muscle, including 250 upregulated proteins and 31 downregulated proteins (Figure 4A). The top upregulated and downregulated pathways in *mdx*^{4cv} muscle have been previously reported in *mdx* mice, demonstrating defects in, for example, cytoskeletal structure and sarcolemmal integrity (20, 21), extracellular matrix organization (22-24), and fatty acid metabolism (25, 26).

In contrast, few proteins displayed significantly elevated or depleted levels in single, dual, or triple AAV-treated *mdx*^{4cv} gastrocnemius muscle compared to WT muscle (Figure 4, B-D). A total of 16 upregulated and 3 downregulated proteins were identified between µDys5-*mdx*^{4cv} and WT mice (Figure 4B). 18 upregulated proteins and 5 downregulated proteins were observed in midi-Dys-*mdx*^{4cv} muscle compared to WT (Figure 4C), while 39 upregulated and 7 downregulated proteins were found between full-Dys-*mdx*^{4cv} and WT mice (Figure 4D).

Further analysis of top upregulated and downregulated DEPs in *mdx*^{4cv} compared to WT gastrocnemius revealed that several cellular processes are dysregulated (Figure 5). For instance, upregulated DEPs in *mdx*^{4cv} muscle are enriched for molecular functions and biological processes including protein and mRNA binding, cytoskeletal structure, supramolecular fiber organization, and regulation of RNA splicing, with cellular compartment enrichment for cytoplasmic, collagen-

containing extracellular matrix, spliceosome, sarcolemmal, and endoplasmic reticulum proteins (Figure 5, A and B). Downregulated DEPs in *mdx*^{4cv} muscles, however, are enriched for molecular functions including nucleosomal DNA binding, fatty acid metabolic processes, and muscle tissue development, with cellular compartment enrichment for DGC, sarcolemmal, cytoplasmic, and euchromatin-enriched proteins (Figure, 5 A and C).

Importantly, several of these defects were partially restored with the dystrophin replacement using AAVMYO1 vectors at variable levels (Figures 5 and 6). For example, treatment with AAV-μDys5 treatment restored the abundance of DGC proteins, including sarcoglycans (β, γ, and δ) and dystroglycans (Figure 3A, 6A, 6B, Supplementary Figure 3 and Supplementary Figure 4), while the dual AAV-midi-Dys and triple AAV-full-Dys treatments resulted in similar patterns of proteomic restoration compared to *mdx*^{4cv} muscle but were slightly less effective in restoring sarcoglycan and dystroglycan levels (Figure 3A, 6A, and 6B). In contrast, levels of α-syntrophin and utrophin were normalized with dual AAV midi-Dys but remain slightly affected with μDys or triple AAV-full-Dys treatments (Figure 6C, 6D, and Supplementary Figure 4), although utrophin levels were variable when assessed by western blot (Supplementary Figure 4).

Similarly, several proteins with elevated abundance in WT muscle displayed reduced abundance in saline-treated *mdx*^{4cv}, whereas dystrophin construct expression mediated by AAV partially or fully restored their cellular enrichment, including protein-arginine deiminase type-2 and myoglobin (Figure 6E), as previously shown for myoglobin (27). In contrast, tubulin beta 6 class V, whose abundance was higher in the saline group, consistent with a previous study (28), was greatly reduced in AAV-treated groups (Figure 6E).

In summary, these data confirm the depletion of the DGC in *mdx*^{4cv} muscle and corroborate other known disease sequelae in dystrophin-deficient muscle, including increased fibrosis and collagen

deposition in the extracellular matrix, whereas μDys and intein-generated midi-Dys and full-Dys, respectively, restored 262, 258, and 235 out of 281 dysregulated proteins, which greatly improved the underlying cellular defects in *mdx*^{4cv} mice.

Dystrophin replacement partially restores biomarkers involved in membrane repair and myogenesis

Severe sarcolemmal fragility and susceptibility to cycles of damage and muscle regeneration represent a hallmark of DMD pathology due to the absence of dystrophin as a structural membrane protein. Disease-specific proteomic alterations in *mdx* skeletal muscle include changes in cytoskeletal, structural, and membrane repair proteins (29). Based on our data demonstrating that more than 85% of *mdx*^{4cv} proteomic alterations exhibit an intermediate or near-complete level of rescue by various-length AAV-Dys treatment, we investigated the impact of μDys5, midi-Dys, and full-Dys expression on membrane trafficking and repair proteins in *mdx*^{4cv} gastrocnemius muscle. A general trend of pathway elevation was observed in *mdx*^{4cv} muscle, with partial restoration across all AAV-Dys treatment groups (Figure 7A). Following this pattern, annexin A1 and annexin A5 levels were increased in *mdx*^{4cv} muscle compared to WT and partially restored by AAV-Dys treatment (Figure 7B). We also observed elevated annexin A4 levels in *mdx*^{4cv} muscle, but only midi-Dys AAV treatment significantly reduced annexin A4 to an intermediate level between WT and dystrophin-deficient muscle (Figure 7B). Dysferlin also displayed elevated levels in saline-*mdx*^{4cv} muscles. While an intermediate restoration was detected in the AAV-treated groups, only dual midi-Dys treatment significantly reduced dysferlin levels compared to saline-*mdx*^{4cv} (Figure 7C and Supplementary Figure 4). Likewise, elevated levels of caveolin-3 and MG53/TRIM72 were found in control *mdx*^{4cv} muscle that were significantly but modestly reduced by AAV treatment (Figure 7C).

225 Furthermore, we analyzed the expression level of proteins implicated in membrane remodeling,
226 trafficking, and cytoskeleton dynamics, such as clathrin light chain A, dynamin-2, and
227 amphiphysin-2 (BIN1). These proteins were enriched in saline-*mdx*^{4cv} muscles with 2-3-fold
228 higher levels compared to WT muscles (Figure 7D). However, variable effects were found with
229 the different dystrophin constructs. For instance, partial restoration was observed with the single
230 AAV-μDys treatment, whereas near-complete normalization of these proteins was obtained with
231 dual or triple AAV approaches (Figure 7D). Conversely, all dystrophin constructs restored the level
232 of galectin-1 to WT levels and significantly reduced galectin-3, which were found 3- and 5-fold
233 higher in saline-treated dystrophic muscles (Figure 7E and F).

234 These observations highlight the impairment of several key proteins involved in different
235 pathways, including myogenesis, membrane repair and remodeling in dystrophin-deficient
236 myofibers, which were rescued to variable extents by dystrophin replacement strategies using
237 single, dual, or triple AAVMYO1.

238 **Incomplete corrections with dystrophin gene therapy**

239 Based on the observation that *mdx*^{4cv} gastrocnemius muscles treated with single, dual, or triple
240 AAV-Dys constructs retain some proteomic features that are distinct from healthy WT muscle
241 (Figure 4), we sought to identify whether AAV split intein Dys treatment results in unique,
242 potentially pathological changes in protein expression and whether the unrestored DEPs in AAV-
243 treated *mdx*^{4cv} muscle are relevant to DMD disease processes. We filtered our dataset for proteins
244 that met the following two criteria: 1) significantly altered in AAV-treated *mdx*^{4cv} muscle compared
245 to WT muscle, and 2) not significantly altered between AAV-treated and untreated *mdx*^{4cv} groups.
246 After filtering, we obtained short lists of unrestored DEPs in μDys5-*mdx*^{4cv}, midi-Dys-*mdx*^{4cv} and
247 full-Dys-*mdx*^{4cv} gastrocnemius muscle (Figure 8, A-C). Several proteins demonstrated depleted

abundance in *mdx*^{4cv} muscle that was not restored by the different dystrophin constructs, including carboxylesterase 1D (gene name *Ces1d*; Figure 8D), spermine oxidase (gene name *Smox*; Figure 8E), tRNA methyltransferase 10 homolog C (gene name *Trmt10c*; Figure 8F), adenosylmethionine decarboxylase (gene name *Amd1*; Figure 8G), and histone H1.2 (gene name *H1-2*; Figure 8H). Levels of several upregulated proteins in *mdx*^{4cv} muscle were not ameliorated or were only partially ameliorated by AAV-dystrophins treatments, including myosin light chain 6B (gene name *Myl6b*; Figure 8I), and heme binding protein 1 (gene name *Hebp1*; Figure 8J). Importantly, the introduction of split-intein dystrophin constructs did not induce unique or deleterious proteomic changes in the *mdx*^{4cv} gastrocnemius muscles. A singular protein, nicotinamide nucleotide transhydrogenase (NNT; gene name *Nnt*), demonstrated expression changes in *mdx*^{4cv} muscle that were more pronounced with AAV-dystrophin treatment; however, NNT expression levels did not display a statistically significant difference between treated and untreated *mdx*^{4cv} muscle (Figure 8K). Only two of the proteins identified as dysregulated in naïve or AAV-treated *mdx*^{4cv} muscle, myosin light chain 4 (gene name *Myl4*) and hypoxanthine-guanine phosphoribosyltransferase (gene name *Hprt1*), were referenced in previous studies involving *mdx* mice (30-33). Notably, a singular protein, eukaryotic translation initiation factor 2D (gene name *Eif2d*), was identified as uniquely altered by AAV treatment (Figure 8L), suggesting a minimal biological impact of injection with the AAV constructs themselves.

Discussion

Genetic mutations in the *DMD* gene have been associated with the development of dystrophinopathies, a group of fatal diseases characterized by progressive degeneration of striated muscles. While the primary cause is the lack of functional dystrophin, leading to fragility of the sarcolemma membrane and high susceptibility to damage from muscle contraction, additional

cellular defects are being revealed through studies involving patient-derived biological material or dystrophin-deficient cellular and animal models (34). A plethora of therapeutic strategies have emerged aiming to deliver or restore the expression of dystrophin or treat downstream disease sequelae by modulating several signaling pathways (35). However, measuring the effectiveness of these therapies was limited to the quantitation of dystrophin protein, the characterization of the general muscle histology, or measuring the mechanical properties of skeletal muscle. Here, we utilized a proteomics method to delineate a global protein expression profile in healthy or dystrophin-deficient murine muscles. Moreover, we used this method to validate the therapeutic outcomes of three different dystrophin replacement strategies in *mdx*^{4cv} mice and compiled a list of unrestored defects that might be used as biomarkers for future studies.

Our dataset confirms the depletion of DGC proteins and demonstrates an overall pattern of elevated expression for membrane trafficking and repair pathway proteins in *mdx*^{4cv} muscle, with partial restoration of some proteins by the different dystrophin constructs expressed via AAV delivery. Lower levels of DGC proteins were previously described in dystrophin-null muscles as a direct consequence of the absence of dystrophin (36, 37), whereas the upregulation of MG53/TRIM72, dysferlin, caveolin-3, utrophin, and members of the annexin family may reflect an adaptive response to increased sarcolemmal membrane fragility and rupture. The function of annexin A4 in sarcolemmal repair has not been clearly defined. However, overexpression of other annexin family members has been observed in DMD muscle as a response to increased membrane fragility and activation of membrane repair processes (38, 39). Interestingly, genetic mutations affecting the expression of dysferlin and caveolin-3 have been associated with the development of muscular dystrophies (40-43). In addition, several reports have shown the molecular interaction of

MG53/TRIM72, dysferlin, and caveolin-3 in muscles and suggested their modulation as a potential therapeutic target in various muscular disorders (44-48).

Similarly, other proteins with essential roles in membrane trafficking and remodeling, including clathrin light chain 1, dynamin-2, and amphiphysin-2 (BIN1), were found expressed at high levels in dystrophin-null *mdx*^{4cv} muscles. These proteins were also linked to the pathogenesis of different congenital myopathies (49, 50). In the last decade, dynamin-2 and BIN1 have been extensively investigated as genetic modifiers in different muscular disorders (51-55), but their role in the pathogenesis of DMD has yet to be characterized. For instance, BIN1 and dynamin-2, as well as dysferlin and caveolin-3, are involved in transverse tubule (T-tubule) formation (56). These invaginations of the sarcoplasmic membrane associate with two sarcoplasmic reticula to form the triads, which are key regulators in excitation-contraction coupling. Early studies suggested the presence of dystrophin in the T-tubules (57, 58), while another study indicated structural and functional defects in the sarcoplasmic reticulum in dystrophin-deficient muscles, contributing to calcium homeostasis defects (59). Although the expression of dystrophin constructs with variable lengths using AAV vectors leads to changes in the expression profiles of the various proteins involved in membrane repair, trafficking, and remodeling, additional studies confirming the restoration of these cellular processes are needed.

Our data confirm the upregulation of galectin-1 and galectin-3. Elevated levels of these proteins have been reported previously in cellular and animal models of DMD, as well as in patient-derived muscle samples (60-62). Recent work has linked galectin-3 to lysosomal damage in two mouse models of muscular dystrophy (62). In particular, AAV–mediated γ-sarcoglycan gene replacement normalized galectin-3 expression in the *Sgcg*$^{-/-}$ mouse model of limb-girdle muscular dystrophy R5 (LGMDR5, γ-sarcoglycanopathy). In contrast, μDys supplementation in *mdx*^{4cv} mice resulted

316 in limited rescue of lysosomal defects, which were hypothesized to arise from elevated galectin-3
317 levels (62). Our proteomic data demonstrate restoration of galectin-3 across all dystrophin
318 constructs tested, including μDys. Differences in μDys sequence, expression cassette, AAV capsid
319 (AAV9 *versus* the myotropic vector AAVMYO), and vector dose may underlie the divergent
320 outcomes observed in *mdx*^{4cv} mice between the two studies. Nevertheless, our dataset lacks
321 histopathological characterization of lysosomal damage–mediated defects. Further studies are
322 warranted to elucidate the impact of these defects in skeletal muscle and to assess the therapeutic
323 potential of different dystrophin constructs.

324 Additionally, using our proteomics approach, we correlated the increase in fibrosis found on
325 muscle sections stained with trichrome to the upregulation of collagen XIVa1, but not other
326 collagen isoforms. Collagen XIVa1 plays a crucial role in the regulation of extracellular matrix
327 (ECM) organization and tissue integrity across various organs and has been linked to fibrotic
328 disease as well as cardiovascular conditions (63). Nonetheless, most studies agree on the primary
329 implication of collagen I (alpha1 and alpha2 chains) and collagen III in the development of fibrosis
330 in skeletal muscles (64-66). The time point chosen in this study (i.e., 5 months of age) is premature
331 to draw robust conclusions about the expression profile of the different collagen forms and their
332 contributions to the mild and early-stage fibrosis found in the muscle sections. Moreover, our data
333 confirmed the upregulation of periostin, which was previously identified as a pro-fibrotic marker
334 in *mdx* mice and other mouse models of muscular dystrophies (67, 68).

335 Furthermore, AAV-mediated delivery and expression of dystrophin constructs did not restore the
336 expression profile of various proteins to wild-type levels. This could be explained by either the
337 mosaic expression of dystrophin in only half of myofibers or the disease status and the age when
338 AAVs were administered (8 weeks old and analysis 3 months post-AAV infusion). At this age,

mdx muscles may have already accumulated cellular, histological, and functional defects due to the absence of dystrophin during muscle development in the embryonic stage, as well as the postnatal phase (69, 70).

It is noteworthy that clinical trials of AAV-μDys also display mosaic expression of μDys and invariably enroll patients who have already begun developing dystrophic pathophysiology. At this stage, in both mice and patients, skeletal muscles have undergone many cycles of degeneration and regeneration crisis, and many, if not all, myofibers have been replaced (71). Previous studies have shown that the downregulation of genes encoding adenosylmethionine decarboxylase (*Amd1*) and spermine oxidase (*Smox*) worsens the myopathy in the tibialis anterior muscle of mice with LAMA2-deficient congenital muscular dystrophy (72). More recent evidence suggests that dysregulated polyamine metabolism also contributes to muscle fiber defects in the context of amyotrophic lateral sclerosis (73). Increased urinary levels of spermine metabolites have been observed in DMD patients for decades (74). However, there is not enough evidence available to support the central role of altered polyamine homeostasis in promoting skeletal muscle pathology in DMD patients. The consequences of unrestored polyamine metabolic enzyme levels in *mdx*^{4cv} gastrocnemius muscle after AAV-dystrophin therapy are, therefore, unknown but unlikely to fully explain residual functional deficits in treated muscle.

In conclusion, this study describes the use of a proteomics approach to study the global protein expression in healthy or dystrophic skeletal muscles. This method can be implemented to validate therapeutic strategies in preclinical and clinical studies and monitor the effectiveness of treatments for muscular disease.

Materials And Methods

Sex as a biological variant:

DMD is an X-linked disease affecting mainly boys. Therefore, only males were used in this study. *mdx*^{4cv} females and males were used for breeding and generating mouse cohorts.

Animals:

Mice were randomized into experimental groups based on availability. They were assigned a serial identification number to conduct a blinded study. These numbers were used throughout the study, and the treatment history of each mouse was determined after completing the data collection.

AAV production

µDys5 (ΔSR2-15, ΔSR18-21, ΔCT), split gp41.1/midiDys (ΔSR5-15) N- or C-terminal constructs, or split dystrophin with split Nrdj1 and split gp41.1 combination were inserted in pAAV containing the muscle-specific M-creatine kinase (CK) 8e expression cassette (CK8e, gift from Dr. Stephen D. Hauschka, University of Washington, Seattle, USA) and a synthetic polyA flanked by two inverted terminal repeats (17, 19). These constructs were packaged in the myotropic AAVMYO1 (gift from Dr. Dirk Grimm, University of Heidelberg, Heidelberg, Germany) vectors using the conventional triple plasmid transfection of Human Embryonic Kidney 293 (HEK293) cells as previously described (75).

AAV administration

8-week-old *mdx*^{4cv} males were anesthetized using isoflurane (Piramal Critical Care) before systemic administration of a low dose of AAVMYO1 into the tail vein (µDys: $2x10^{13}$ vg/kg, midi-Dys: $1x10^{13}$ vg/kg of each vector, full-Dys: $1.33x10^{13}$ vg/kg of each vector). As a control, a

subgroup was injected with sterile saline. Once AAV or saline solutions were successfully administered, mice were kept in a warm cage and monitored for 1 hour.

Muscle histology analysis

Gastrocnemius muscles were isolated from 5-month-old wild-type or *mdx*^{4cv} mice and flash-frozen using liquid nitrogen-cooled isopentane. 10µm cross-sections were prepared using a cryostat (Leica CM1850) and stained for Hematoxylin and Eosin (H&E) or Trichrome. Whole sections were imaged with the Hamamatsu NanoZoomer slide scanner, and the most representative section was presented in this study. Other sections were immunolabeled overnight with antibodies against dystrophin N-terminal (homemade rabbit 246 (76)), gamma sarcoglycan (NCL-g-SARC, Leica Biosystems), beta dystroglycan (NCL-b-DG, Leica Biosystems), periostin (ab1404150, Abcam), myosin heavy chains type I (BA-D5, DSHB), type IIa (SC-71, DSHB), type IIb (BF-F3, DSHB), or Laminin2 (L0663 Rat, Sigma) diluted [1:100] in solutions containing Tris Buffered Salin (TBS)-Tween and 5% Bovine Serum Albumin. Secondary antibodies using goat anti-rabbit Alexa790 (111-655-144, Jackson ImmunoResearch), goat anti-rabbit Alexa488 (111-545-144, Jackson ImmunoResearch), goat anti-mouse IgG2a Alexa488 (115-547-186, Jackson ImmunoResearch), goat anti-rabbit Alexa594 mouse IgG2b (115-587-187, Jackson ImmunoResearch), goat anti-mouse IgG2b Alexa350 (A21140, Invitrogen), goat anti-mouse IgM Alexa488 (115-545-020, Jackson ImmunoResearch), goat anti-mouse IgG1 (115-587-185, Jackson ImmunoResearch) or goat anti-rat Alexa594 (A11007, Invitrogen) were incubated for 2 h diluted in [1:100] in solutions containing TBS-Tween and 5% Bovine Serum Albumin. Slides were mounted using Immu-Mount (Epredia), and images were captured on the Nikon Eclipse 90i Microscope. The myofiber size and minimal fiber diameter (miniFeret) were determined from laminin-positive sections. The percentage of dystrophin-positive myofibers was quantified using sections stained with dystrophin

and laminin antibodies, while dystrophin-positive fiber type percentage was quantified from section quadruply stained with dystrophin and myosin heavy chains. The fibrosis area was measured using sections stained with Trichrome. Periostin area was quantified from sections stained with anti-periostin antibodies. Fiji image analysis software (version 2.0.0-rc-68/1.52g) was used to quantify all the histology parameters cited above.

Protein extraction, digestion, and peptide isobaric labeling

Frozen gastrocnemius muscle tissue pieces (20-25mg) were processed using a Percellys Cryolys Evolution bead beater (Bertin Technologies). Tissue samples were weighed in Percellys tissue homogenizing CKMix tubes (Bertin Technologies) and protein extraction buffer [7M urea, 2M thiourea, 0.4M Tris pH 8.0, 20% (v/v) acetonitrile, 10mM tris (2-carboxyethyl) phosphine (TCEP), 40mM chloroacetamide, and 1µl/100ul buffer Pierce Universal Nuclease (Thermo Fisher Scientific)] was added at a ratio of 9ul lysis buffer per 1mg tissue. A 150µl aliquot of each sample was transferred to a PCT tube with a 150µl cap for the Barocycler NEP2320 (Pressure Biosciences, Inc., South Easton, MA) and cycled between 35 kPSI for 20 sec and 0 kPSI for 10 sec. for 60 cycles at 37°C. After barocycling, the samples were centrifuged at 15,000xg for 10 min. The samples were transferred to new 1.5mL microfuge Eppendorf Protein LoBind tubes. Aliquots for each sample were taken for protein concentration determination by Bradford assay.

A bridged pooled normalizing sample was made for two TMTpro 16plex (Tandem Mass Tag, Thermo Fisher Scientific, Waltham, MA) experiments. The pooled sample was composed of equal µg aliquots of each GAS sample. An 18µg aliquot of each sample and pooled sample was transferred to a new 1.5mL Eppendorf Protein LoBind tube and brought to the same volume with extraction buffer. The samples were diluted fivefold with LC-MS grade water. Next, trypsin (Promega, Madison, WI) was added in a 1:40 ratio of trypsin to total protein. Samples were

incubated at 37°C overnight, then were acidified with 0.3% (v/v) formic acid. Samples were cleaned using a MCX Stage tip and eluates were vacuum dried. Samples were resuspended with 0.1M triethylammonium bicarbonate, pH 8.5, to a final protein concentration of 1μg/μL.

For stable isotope labeling, a 14μg aliquot for each sample was made and assigned a channel within a TMTpro 16plex. The samples were labeled with TMTpro 16plex isobaric label reagent in a 1:10 ratio of μg protein to μg TMTpro 16plex label according to the manufacturer's instructions. Isobaric tag-labeled samples within the same experimental screen were multiplexed together into a new 1.5mL Eppendorf tube, then vacuum dried and cleaned with a 1mL SepPak C18 solid phase extraction cartridge (Waters Corporation, Milford, MA). Each TMTpro 16plex sample was vacuum dried, resuspended in 20 mM ammonium formate, pH 10, 98% (v/v) water and 2% (v/v) acetonitrile and fractionated offline by high pH C18 reversed-phase chromatography as previously described (77). After fractionation, concatenated peptide fractions were C18 Stage tipped (78) and eluates were dried *in vacuo*.

Mass spectrometry data acquisition

Skeletal muscle TMTpro 16plex proteomics experiments were performed at the University of Minnesota in collaboration with the Center for Metabolomics and Proteomics (CMSP) departmental core facility. Gastrocnemius muscle was extracted from five experimental groups of mice, including male WT (C57BL/6), untreated *mdx*^{4cv} (B6Ros.Cg-Dmd$^{mdx\text{-}4Cv}$/J**),** μDys, midi-Dys, and full-Dys mice. Mice treated with low-dose AAV gene therapy constructs were sacrificed 3 months after treatment, and untreated WT and *mdx*^{4cv} mice were age-matched with treated mice. Each group consisted of n=6 biological replicates for a total of 30 samples. Two TMTpro 16plex screens were run sequentially to include all samples split equally between each screen, along with a pooled normalization control sample included in each screen. Peptide pellets were resuspended

in solution consisting of 95% water, 5% acetonitrile, and 0.1% formic acid. The peptide mixture was vortexed for 45 seconds and centrifuged for 2 minutes at 4,000xg. Data was collected on a Thermo Orbitrap Eclipse™ mass spectrometer coupled to a Dionex™ Ultimate™ 3000 RSLCnano LC pump. Peptides from 17% (2µL) of each concatenated set of fractions were separated using a 199-min gradient at 0.315-0.325µL/min with a 0-90% Buffer B gradient at a column temperature of 55°C on a C18-AQ ReproSil-Pur column measuring 400mm with an internal diameter of 100µm, 1.9µm resin size, and 120Å pore size (Dr. Maisch GmbH Ammerbuch, Germany). Buffer A consisted of water with 0.1% (v/v) formic acid and Buffer B consisted of acetonitrile with 0.1% (v/v) formic acid. High-field asymmetric-waveform ion mobility spectroscopy (FAIMS) was enabled during experimental acquisition with the following compensation voltage (CV) settings: -45 V, -60 V, and -75 V. Voltage was kept at 2.1 kV for positive ion mode and the ion transfer tube temperature was set to 275°C. At the MS1 stage, the mass spectrometer scanned masses in the range of 400-1400 m/z at a resolution of 120K with an AGC target of 4.0E5 over a 50ms maximal injection time. At the MS2 stage, ions were fragmented by high-energy collisional dissociation (HCD) with a collision energy of 38% at a detector resolution of 50K with an AGC target of 1.25E+5 (250% relative to default) over a 150ms maximal injection time, and the Fourier transform first mass mode was fixed at 110 *m/z*.

Proteomics peptide spectrum matching and quantification

Raw MS files were processed by CMSP in Proteome Discoverer v3.1 (Thermo Fisher Scientific, Rockford, IL, USA). Peptide identification was performed by searching HCD MS/MS files against the UniProtKB/Swiss-Prot *mus musculus* database (UP000000589; accessed August 18, 2023) appended with custom dystrophin sequences from AAV-Myo1 µDys5, midi-Dys, and flDys constructs. Database search files were merged with a common lab contaminant database

(https://github.com/HaoGroup-ProtContLib) with the Sequest HT search engine and a 1% false discovery rate (FDR) was set for peptide-to-spectrum matches using the Percolator algorithm in Proteome Discoverer v3.1. The following parameters were used for spectral processing: MS1 tolerance of 20ppm, MS2 tolerance of 0.08 Da, trypsin (full) digestion with a maximum of two missed cleavage, minimum peptide length of 6 and maximum peptide length of 50, with 10 maximum peptides reported. Cysteine carbamidomethylation was set as a static modification, while TMTpro lysine and N-terminal modifications, asparagine and glutamine deamidation, methionine oxidation, pyro-glutamic acid, N-terminal acetylation, methionine-loss, and methionine loss with acetylation were set as dynamic modifications in Sequest. Only protein identifications with high FDR confidence (FDR<1%) and containing 2 or more peptides were accepted. Reporter ion quantification was conducted using the TMTpro 16plex Lot-YD372049 quantification method with a peak integration tolerance of 20ppm and the most confident centroid method. Unique and razor peptides were used for quantification. All peptides were used for normalization and protein roll-up, and scaling was performed for inter-screen data normalization using a pooled average control sample. Hypothesis testing was performed using t-test (background based) for pairwise ratios. Grubbs' test was used to identify and exclude single outlier datapoints.

Western blot:

Proteins were extracted from gastrocnemius muscles using radioimmunoprecipitation analysis buffer (RIPA) supplemented with 1 mM PMSF and a 4% protease inhibitor cocktail (P8340, Sigma). Total protein concentration was determined using the Pierce BCA assay kit (ThermoFisher). Samples were denatured at 100 °C for 10 min, then 30 µg of protein lysates were separated in NuPage 4-12% Bis-Tris polyacrylamide gels (Invitrogen) using 165 volts for 1h at room temperature. Protein transfer to 0.45 µm PVDF membranes (Amersham hybond) was

performed at 120 volts at 4 °C for 2 h. Membranes were blocked for 2 h in TBS containing 5% non-fat dry milk and 0.005% Tween20 before overnight incubation with antibodies against utrophin (rabbit (79), gift from Froehner lab, University of Washington, Seattle, USA), dysferlin (Hamlet-CE, Leica Biosystems), gamma sarcoglycan (NCL-g-SARC, Leica Biosystems), or GAPDH (rabbit, Sigma G9545) as a loading control. Secondary antibodies coupled to horseradish peroxidase were anti-mouse IgG2b (115-035-207, Jackson ImmunoResearch), anti-mouse IgG1 (115-035-205, Jackson ImmunoResearch), or goat anti-rabbit (111-035-144, Jackson ImmunoResearch). Blots were incubated for 2 h at room temperature before visualization using Clarity Western ECL substrate (BioRad) in the Chemidoc MP imaging system (BioRad). The relative expression was determined by band densitometry measurements on unsaturated images using Fiji image analysis software.

Data availability:

Source data to interpret, verify, and extend this research are provided in this paper. The mass spectrometry proteomics data have been deposited to the ProteomeXchange Consortium via the PRIDE (80) partner repository with the dataset identifier PXD062324. Source data are provided in this paper. R script used to generate plots, filter, and analyze data is publicly available at: https://github.com/joh18358/Split-intein-mdx-proteomics.

Statistics

Comparisons between all experimental groups were performed using one-way ANOVA statistical analysis with Tukey's multiple comparisons correction. Scaled protein abundances were used to calculate pairwise fold changes based on the geometric means of all biological replicates from each sample group. Fold changes were calculated for pairwise comparisons between the following groups: *mdx*^{4cv}/WT, AAVMYO1 µDys5-treated *mdx*^{4cv}/WT, AAVMYO1 midi-Dys-treated

mdx^{4cv}/WT, AAVMYO1 flDys-treated *mdx*^{4cv}/WT, *mdx*^{4cv}/μDys5-treated *mdx*^{4cv}, *mdx*^{4cv}/midi-Dys-treated *mdx*^{4cv}, *mdx*^{4cv}/flDys-treated *mdx*^{4cv}, μDys5-treated *mdx*^{4cv}/midi-Dys-treated *mdx*^{4cv}, μDys5-treated *mdx*^{4cv}/flDys-treated *mdx*^{4cv}, and midi-Dys-treated *mdx*^{4cv}/flDys-treated *mdx*^{4cv}. A two-way unpaired Student's t-test was used to calculate p-values for pairwise fold changes, and the Benjamini Hochberg method was used to control the false discovery rate (FDR). Corrected p-values were log-transformed and plotted against log-transformed fold change values to obtain volcano plots generated in R using the tidyverse package, and a minimum corrected p-value cutoff of 0.05 and minimum relative fold change cutoff of ±1 was applied to identify differentially expressed proteins (DEPs) in pairwise comparisons. Comparisons between all experimental groups were performed using one-way ANOVA statistical analysis with Tukey's multiple comparisons correction. Full protein quantification datasets generated in Proteome Discoverer and lists of DEPs were imported to R for data filtering and visualization using the gplots, VennDiagram, and dplyr packages. Venn diagrams were used to obtain lists of overlapping and non-overlapping DEPs between distinct two-group comparisons. Proteins with missing values for pooled samples in one or both screens were excluded from further analysis. Functional enrichment analysis was performed using Gorilla (81) and g:Profiler (82). For DEP gene ontology analysis, the target set included the DEP list and the background set the *Mus musculus* reference proteome. PCA plots were generated in R using the ggfortify package. One-way ANOVA statistical analysis and dataset filtering were performed in R. Bar graphs, GO enrichment visualizations, and heat maps for DEPs of interest were performed in GraphPad Prism, version 10.2.

Study approval:

All animal experiments were approved by the University of Washington's Institutional Animal Care and Use Committee (IACUC).

Author contributions:

H.T and J.S.C designed the AAV treatment and strategy. E.E.J and J.M.E conceptualize the proteomics study. H.T produced and purified the AAV, injected mice, and collected muscle samples. E.E.J prepared the muscle samples and proteins for proteomics analysis and performed the statistical and bioinformatic analysis. H.T and T.R.R analyzed the muscle histology. H.T and E.E.J wrote the manuscript. J.M.E and J.S.C provided reagents and edited the manuscript.

Funding support:

This work is the result of NIH funding, in whole or in part, and is subject to the NIH Public Access Policy. Through acceptance of this federal funding, the NIH has been given a right to make the work publicly available in PubMed Central.

This work was supported by research grants from the Muscular Dystrophy Association (MDA, USA 1060372), the Association Française Contre Les Myopathies (AFM-Telethon, 24777), The Diabetes Research Center and the Wellstone Center at the University of Washington (P30 DK017047 and P50 AR065139), and the US Department of Defense (MD220097). H.T was supported by fellowships from Bettencourt-Schueller Foundation, Philippe Foundation, and Association Française Contre Les Myopathies (AFM-Telethon). This work was also supported by the National Institutes of Health Minnesota Muscle Training Grant 5T32AR007612 to E.E.J. and by NIH grant 5R01AR042423 to J.M.E. The Orbitrap Eclipse instrumentation platform used for proteomics data acquisition in this work was purchased through High-end Instrumentation Grant S10OD028717 from the NIH.

Acknowledgments:

We thank the Viral Vector Core of the Sen. Paul D. Wellstone Muscular Dystrophy Specialized Research Center, the Histology and Imaging Core at the University of Washington, and the

University of Minnesota Center for Metabolomics and Proteomics for the excellent technical assistance. We thank Dr. Dirk Grimm (University of Heidelberg) and Dr. Stephen D. Hauschka (University of Washington) for providing the AAVMYO1 and CK8e plasmids, respectively.

References:

1. Emery AE. The muscular dystrophies. *Lancet*. 2002;359(9307):687-95.
2. Ray PN, Belfall B, Duff C, Logan C, Kean V, Thompson MW, et al. Cloning of the breakpoint of an X;21 translocation associated with Duchenne muscular dystrophy. *Nature*. 1985;318(6047):672-5.
3. Monaco AP, Bertelson CJ, Middlesworth W, Colletti CA, Aldridge J, Fischbeck KH, et al. Detection of deletions spanning the Duchenne muscular dystrophy locus using a tightly linked DNA segment. *Nature*. 1985;316(6031):842-5.
4. Hoffman EP, Brown RH, Jr., and Kunkel LM. Dystrophin: the protein product of the Duchenne muscular dystrophy locus. *Cell*. 1987;51(6):919-28.
5. Ervasti JM, and Campbell KP. Membrane Organization of the Dystrophin-Glycoprotein Complex. *Cell*. 1991;66(6):1121-31.
6. Ervasti JM, and Campbell KP. A Role for the Dystrophin-Glycoprotein Complex as a Transmembrane Linker between Laminin and Actin. *J Cell Biol*. 1993;122(4):809-23.
7. Bengtsson NE, Tasfaout H, and Chamberlain JS. The road towards AAV-mediated gene therapy of Duchenne muscular dystrophy. *Mol Ther*. 2025.
8. Srivastava A, Lusby EW, and Berns KI. Nucleotide sequence and organization of the adeno-associated virus 2 genome. *J Virol*. 1983;45(2):555-64.
9. England SB, Nicholson LV, Johnson MA, Forrest SM, Love DR, Zubrzycka-Gaarn EE, et al. Very mild muscular dystrophy associated with the deletion of 46% of dystrophin. *Nature*. 1990;343(6254):180-2.
10. Harper SQ, Hauser MA, DelloRusso C, Duan D, Crawford RW, Phelps SF, et al. Modular flexibility of dystrophin: implications for gene therapy of Duchenne muscular dystrophy. *Nat Med*. 2002;8(3):253-61.
11. Davies KE, and Vogt J. Long-term clinical follow-up of a family with Becker muscular dystrophy associated with a large deletion in the DMD gene. *Neuromuscul Disord*. 2024;39:5-9.
12. Phelps SF, Hauser MA, Cole NM, Rafael JA, Hinkle RT, Faulkner JA, et al. Expression of full-length and truncated dystrophin mini-genes in transgenic mdx mice. *Hum Mol Genet*. 1995;4(8):1251-8.
13. Banks GB, Judge LM, Allen JM, and Chamberlain JS. The polyproline site in hinge 2 influences the functional capacity of truncated dystrophins. *PLoS Genet*. 2010;6(5):e1000958.
14. Gregorevic P, Allen JM, Minami E, Blankinship MJ, Haraguchi M, Meuse L, et al. rAAV6-microdystrophin preserves muscle function and extends lifespan in severely dystrophic mice. *Nat Med*. 2006;12(7):787-9.
15. Ramos JN, Hollinger K, Bengtsson NE, Allen JM, Hauschka SD, and Chamberlain JS. Development of Novel Micro-dystrophins with Enhanced Functionality. *Mol Ther*. 2019;27(3):623-35.
16. Birch SM, Lawlor MW, Conlon TJ, Guo LJ, Crudele JM, Hawkins EC, et al. Assessment of systemic AAV-microdystrophin gene therapy in the GRMD model of Duchenne muscular dystrophy. *Sci Transl Med*. 2023;15(677):eabo1815.

17. Tasfaout H, Halbert CL, McMillen TS, Allen JM, Reyes TR, Flint GV, et al. Split intein-mediated protein trans-splicing to express large dystrophins. *Nature*. 2024;632(8023):192-200.
18. Shah NH, and Muir TW. Inteins: Nature's Gift to Protein Chemists. *Chem Sci*. 2014;5(1):446-61.
19. Tasfaout H, McMillen, T. S., Reyes T. R., Halbert, C. L., Tian R., Regnier M., Chamberlain J. S. . Expression of full-length dystrophin reverses muscular dystrophy defects in young and old mdx4cv mice. *Journal of Clinical Investigation*. In press.
20. Ibraghimov-Beskrovnaya O, Ervasti JM, Leveille CJ, Slaughter CA, Sernett SW, and Campbell KP. Primary structure of dystrophin-associated glycoproteins linking dystrophin to the extracellular matrix. *Nature*. 1992;355(6362):696-702.
21. Ervasti JM, and Campbell KP. A role for the dystrophin-glycoprotein complex as a transmembrane linker between laminin and actin. *J Cell Biol*. 1993;122(4):809-23.
22. McCourt JL, Stearns-Reider KM, Mamsa H, Kannan P, Afsharinia MH, Shu C, et al. Multi-omics analysis of sarcospan overexpression in mdx skeletal muscle reveals compensatory remodeling of cytoskeleton-matrix interactions that promote mechanotransduction pathways. *Skelet Muscle*. 2023;13(1):1.
23. Wang X, Chen J, Homma ST, Wang Y, Smith GR, Ruf-Zamojski F, et al. Diverse effector and regulatory functions of fibro/adipogenic progenitors during skeletal muscle fibrosis in muscular dystrophy. *iScience*. 2023;26(1):105775.
24. Xin J, and Liu S. Identifying hub genes and dysregulated pathways in Duchenne muscular dystrophy. *Int J Neurosci*. 2025;135(4):375-87.
25. Kalkan H, Pagano E, Paris D, Panza E, Cuozzo M, Moriello C, et al. Targeting gut dysbiosis against inflammation and impaired autophagy in Duchenne muscular dystrophy. *EMBO Mol Med*. 2023;15(3):e16225.
26. Tsonaka R, Seyer A, Aartsma-Rus A, and Spitali P. Plasma lipidomic analysis shows a disease progression signature in mdx mice. *Sci Rep*. 2021;11(1):12993.
27. Olthoff JT, Lindsay A, Abo-Zahrah R, Baltgalvis KA, Patrinostro X, Belanto JJ, et al. Loss of peroxiredoxin-2 exacerbates eccentric contraction-induced force loss in dystrophin-deficient muscle. *Nat Commun*. 2018;9(1):5104.
28. Randazzo D, Khalique U, Belanto JJ, Kenea A, Talsness DM, Olthoff JT, et al. Persistent upregulation of the beta-tubulin tubb6, linked to muscle regeneration, is a source of microtubule disorganization in dystrophic muscle. *Hum Mol Genet*. 2019;28(7):1117-35.
29. Rayavarapu S, Coley W, Cakir E, Jahnke V, Takeda S, Aoki Y, et al. Identification of disease specific pathways using in vivo SILAC proteomics in dystrophin deficient mdx mouse. *Mol Cell Proteomics*. 2013;12(5):1061-73.
30. Heezen LGM, Abdelaal T, van Putten M, Aartsma-Rus A, Mahfouz A, and Spitali P. Spatial transcriptomics reveal markers of histopathological changes in Duchenne muscular dystrophy mouse models. *Nat Commun*. 2023;14(1):4909.
31. Boccanegra B, Lenti R, Mantuano P, Conte E, Tulimiero L, Piercy RJ, et al. Determination of qPCR reference genes suitable for normalizing gene expression in a novel model of Duchenne muscular dystrophy, the D2-mdx mouse. *PLoS One*. 2024;19(11):e0310714.

32. Hildyard JCW, Finch AM, and Wells DJ. Identification of qPCR reference genes suitable for normalizing gene expression in the mdx mouse model of Duchenne muscular dystrophy. *PLoS One*. 2019;14(1):e0211384.
33. Hildyard JCW, Taylor-Brown F, Massey C, Wells DJ, and Piercy RJ. Determination of qPCR Reference Genes Suitable for Normalizing Gene Expression in a Canine Model of Duchenne Muscular Dystrophy. *J Neuromuscul Dis*. 2018;5(2):177-91.
34. Duan D, Goemans N, Takeda S, Mercuri E, and Aartsma-Rus A. Duchenne muscular dystrophy. *Nat Rev Dis Primers*. 2021;7(1):13.
35. Heydemann A, and Siemionow M. A Brief Review of Duchenne Muscular Dystrophy Treatment Options, with an Emphasis on Two Novel Strategies. *Biomedicines*. 2023;11(3).
36. Li D, Long C, Yue Y, and Duan D. Sub-physiological sarcoglycan expression contributes to compensatory muscle protection in mdx mice. *Hum Mol Genet*. 2009;18(7):1209-20.
37. Hoyte K, Jayasinha V, Xia B, and Martin PT. Transgenic overexpression of dystroglycan does not inhibit muscular dystrophy in mdx mice. *Am J Pathol*. 2004;164(2):711-8.
38. Croissant C, Carmeille R, Brevart C, and Bouter A. Annexins and Membrane Repair Dysfunctions in Muscular Dystrophies. *Int J Mol Sci*. 2021;22(10).
39. Swaggart KA, Demonbreun AR, Vo AH, Swanson KE, Kim EY, Fahrenbach JP, et al. Annexin A6 modifies muscular dystrophy by mediating sarcolemmal repair. *Proc Natl Acad Sci U S A*. 2014;111(16):6004-9.
40. Bashir R, Britton S, Strachan T, Keers S, Vafiadaki E, Lako M, et al. A gene related to Caenorhabditis elegans spermatogenesis factor fer-1 is mutated in limb-girdle muscular dystrophy type 2B. *Nat Genet*. 1998;20(1):37-42.
41. Liu J, Aoki M, Illa I, Wu C, Fardeau M, Angelini C, et al. Dysferlin, a novel skeletal muscle gene, is mutated in Miyoshi myopathy and limb girdle muscular dystrophy. *Nat Genet*. 1998;20(1):31-6.
42. Minetti C, Sotgia F, Bruno C, Scartezzini P, Broda P, Bado M, et al. Mutations in the caveolin-3 gene cause autosomal dominant limb-girdle muscular dystrophy. *Nat Genet*. 1998;18(4):365-8.
43. Betz RC, Schoser BG, Kasper D, Ricker K, Ramirez A, Stein V, et al. Mutations in CAV3 cause mechanical hyperirritability of skeletal muscle in rippling muscle disease. *Nat Genet*. 2001;28(3):218-9.
44. Cai C, Weisleder N, Ko JK, Komazaki S, Sunada Y, Nishi M, et al. Membrane repair defects in muscular dystrophy are linked to altered interaction between MG53, caveolin-3, and dysferlin. *J Biol Chem*. 2009;284(23):15894-902.
45. Weisleder N, Takizawa N, Lin P, Wang X, Cao C, Zhang Y, et al. Recombinant MG53 protein modulates therapeutic cell membrane repair in treatment of muscular dystrophy. *Sci Transl Med*. 2012;4(139):139ra85.
46. He B, Tang RH, Weisleder N, Xiao B, Yuan Z, Cai C, et al. Enhancing muscle membrane repair by gene delivery of MG53 ameliorates muscular dystrophy and heart failure in delta-Sarcoglycan-deficient hamsters. *Mol Ther*. 2012;20(4):727-35.

47. Paleo BJ, McElhanon KE, Bulgart HR, Banford KK, Beck EX, Sattler KM, et al. Reduced Sarcolemmal Membrane Repair Exacerbates Striated Muscle Pathology in a Mouse Model of Duchenne Muscular Dystrophy. *Cells*. 2022;11(9).
48. Han R, Rader EP, Levy JR, Bansal D, and Campbell KP. Dystrophin deficiency exacerbates skeletal muscle pathology in dysferlin-null mice. *Skelet Muscle*. 2011;1(1):35.
49. Nicot AS, Toussaint A, Tosch V, Kretz C, Wallgren-Pettersson C, Iwarsson E, et al. Mutations in amphiphysin 2 (BIN1) disrupt interaction with dynamin 2 and cause autosomal recessive centronuclear myopathy. *Nat Genet*. 2007;39(9):1134-9.
50. Bitoun M, Maugenre S, Jeannet PY, Lacene E, Ferrer X, Laforet P, et al. Mutations in dynamin 2 cause dominant centronuclear myopathy. *Nat Genet*. 2005;37(11):1207-9.
51. Lionello VM, Kretz C, Edelweiss E, Crucifix C, Gomez-Oca R, Messaddeq N, et al. BIN1 modulation in vivo rescues dynamin-related myopathy. *Proc Natl Acad Sci U S A*. 2022;119(9).
52. Cowling BS, Chevremont T, Prokic I, Kretz C, Ferry A, Coirault C, et al. Reducing dynamin 2 expression rescues X-linked centronuclear myopathy. *J Clin Invest*. 2014;124(3):1350-63.
53. Tasfaout H, Buono S, Guo S, Kretz C, Messaddeq N, Booten S, et al. Antisense oligonucleotide-mediated Dnm2 knockdown prevents and reverts myotubular myopathy in mice. *Nat Commun*. 2017;8:15661.
54. Cowling BS, Prokic I, Tasfaout H, Rabai A, Humbert F, Rinaldi B, et al. Amphiphysin (BIN1) negatively regulates dynamin 2 for normal muscle maturation. *J Clin Invest*. 2017;127(12):4477-87.
55. Fugier C, Klein AF, Hammer C, Vassilopoulos S, Ivarsson Y, Toussaint A, et al. Misregulated alternative splicing of BIN1 is associated with T tubule alterations and muscle weakness in myotonic dystrophy. *Nat Med*. 2011;17(6):720-5.
56. Al-Qusairi L, and Laporte J. T-tubule biogenesis and triad formation in skeletal muscle and implication in human diseases. *Skelet Muscle*. 2011;1(1):26.
57. Watkins SC, Hoffman EP, Slayter HS, and Kunkel LM. Immunoelectron microscopic localization of dystrophin in myofibres. *Nature*. 1988;333(6176):863-6.
58. Hoffman EP, Knudson CM, Campbell KP, and Kunkel LM. Subcellular fractionation of dystrophin to the triads of skeletal muscle. *Nature*. 1987;330(6150):754-8.
59. Bellinger AM, Reiken S, Carlson C, Mongillo M, Liu X, Rothman L, et al. Hypernitrosylated ryanodine receptor calcium release channels are leaky in dystrophic muscle. *Nat Med*. 2009;15(3):325-30.
60. Cerri DG, Rodrigues LC, Stowell SR, Araujo DD, Coelho MC, Oliveira SR, et al. Degeneration of dystrophic or injured skeletal muscles induces high expression of Galectin-1. *Glycobiology*. 2008;18(11):842-50.
61. Marotta M, Ruiz-Roig C, Sarria Y, Peiro JL, Nunez F, Ceron J, et al. Muscle genome-wide expression profiling during disease evolution in mdx mice. *Physiol Genomics*. 2009;37(2):119-32.

62. Jaber A, Palmieri L, Bakour R, Bourg N, Hong AV, Lachiver E, et al. Lysosomal damage is a therapeutic target in Duchenne muscular dystrophy. *Sci Adv.* 2025;11(43):eadv6805.
63. Tao G, Levay AK, Peacock JD, Huk DJ, Both SN, Purcell NH, et al. Collagen XIV is important for growth and structural integrity of the myocardium. *J Mol Cell Cardiol.* 2012;53(5):626-38.
64. Foidart M, Foidart JM, and Engel WK. Collagen localization in normal and fibrotic human skeletal muscle. *Arch Neurol.* 1981;38(3):152-7.
65. Alexakis C, Partridge T, and Bou-Gharios G. Implication of the satellite cell in dystrophic muscle fibrosis: a self-perpetuating mechanism of collagen overproduction. *Am J Physiol Cell Physiol.* 2007;293(2):C661-9.
66. Duance VC, Restall DJ, Beard H, Bourne FJ, and Bailey AJ. The location of three collagen types in skeletal muscle. *FEBS Lett.* 1977;79(2):248-52.
67. Lorts A, Schwanekamp JA, Baudino TA, McNally EM, and Molkentin JD. Deletion of periostin reduces muscular dystrophy and fibrosis in mice by modulating the transforming growth factor-beta pathway. *Proc Natl Acad Sci U S A.* 2012;109(27):10978-83.
68. Trundle J, Cernisova V, Boulinguiez A, Lu-Nguyen N, Malerba A, and Popplewell L. Expression of the Pro-Fibrotic Marker Periostin in a Mouse Model of Duchenne Muscular Dystrophy. *Biomedicines.* 2024;12(1).
69. Merrick D, Stadler LK, Larner D, and Smith J. Muscular dystrophy begins early in embryonic development deriving from stem cell loss and disrupted skeletal muscle formation. *Dis Model Mech.* 2009;2(7-8):374-88.
70. Granet JA, Robertson R, Cusmano AA, Filippelli RL, Lorenz TO, Li S, et al. Muscle stem cells in Duchenne muscular dystrophy exhibit molecular impairments and altered cell fate trajectories impacting regenerative capacity. *Cell Death Dis.* 2025;16(1):437.
71. DiMario JX, Uzman A, and Strohman RC. Fiber regeneration is not persistent in dystrophic (MDX) mouse skeletal muscle. *Dev Biol.* 1991;148(1):314-21.
72. Kemaladewi DU, Benjamin JS, Hyatt E, Ivakine EA, and Cohn RD. Increased polyamines as protective disease modifiers in congenital muscular dystrophy. *Hum Mol Genet.* 2018;27(11):1905-12.
73. Ruggieri V, Scaricamazza S, Bracaglia A, D'Ercole C, Parisi C, D'Angelo P, et al. Polyamine metabolism dysregulation contributes to muscle fiber vulnerability in ALS. *Cell Rep.* 2025;44(1):115123.
74. Russell DH, and Stern LZ. Altered polyamine excretion in Duchenne muscular dystrophy. *Neurology.* 1981;31(1):80-3.
75. Halbert CL, Allen JM, and Chamberlain JS. AAV6 Vector Production and Purification for Muscle Gene Therapy. *Methods Mol Biol.* 2018;1687:257-66.
76. Rafael JA, Cox GA, Corrado K, Jung D, Campbell KP, and Chamberlain JS. Forced expression of dystrophin deletion constructs reveals structure-function correlations. *J Cell Biol.* 1996;134(1):93-102.
77. Chaanine AH, Higgins L, Markowski T, Harman J, Kachman M, Burant C, et al. Multi-Omics Approach Profiling Metabolic Remodeling in Early Systolic Dysfunction and in Overt Systolic Heart Failure. *Int J Mol Sci.* 2021;23(1).

78. Rappsilber J, Ishihama Y, and Mann M. Stop and go extraction tips for matrix-assisted laser desorption/ionization, nanoelectrospray, and LC/MS sample pretreatment in proteomics. *Anal Chem*. 2003;75(3):663-70.
79. Kramarcy NR, Vidal A, Froehner SC, and Sealock R. Association of utrophin and multiple dystrophin short forms with the mammalian M(r) 58,000 dystrophin-associated protein (syntrophin). *J Biol Chem*. 1994;269(4):2870-6.
80. Perez-Riverol Y, Bandla C, Kundu DJ, Kamatchinathan S, Bai J, Hewapathirana S, et al. The PRIDE database at 20 years: 2025 update. *Nucleic Acids Res*. 2025;53(D1):D543-D53.
81. Eden E, Navon R, Steinfeld I, Lipson D, and Yakhini Z. GOrilla: a tool for discovery and visualization of enriched GO terms in ranked gene lists. *BMC Bioinformatics*. 2009;10:48.
82. Raudvere U, Kolberg L, Kuzmin I, Arak T, Adler P, Peterson H, et al. g:Profiler: a web server for functional enrichment analysis and conversions of gene lists (2019 update). *Nucleic Acids Res*. 2019;47(W1):W191-W8.

Table 1: Dystrophin peptide sequences used in spectrum matching and quantifying endogenous murine full-length dystrophin (WT dystrophin) or transgenic/human dystrophin constructs delivered by AAVMYO1 vectors (μDys5, midi-Dys, and full-Dys constructs). Mismatched residues of human *versus* murine sequences are underlined.

	Peptide ID	Peptide Sequence	Location (encoding exon)	Data represented in
Peptide sequences specific to full-length dystrophin (WT dystrophin and full-Dys construct)	Peptide F1	ELHEEAVR	Spectrin Repeat 9 (exon 29-30)	**Figure 2B**
	Peptide F2	VLSQIDVAQK	Spectrin Repeat 10 (exon 31-32)	
	Peptide F3	SEVEMVIK	Spectrin Repeat 11 (exon 33)	
	Peptide F4	ETLVEDK	Spectrin Repeat 12 (exon 35)	
	Peptide F5	QQLLQTK	Spectrin Repeat 14 (exon 39)	
Peptide sequences specific to transgenic/human dystrophins (shared between μDys5, midi-Dys, and full-Dys constructs)	Peptide hD1	WVNAQFSK	Calponin-homology (CH) 1 (exon 2)	**Figure 2C**
	Peptide hD2	YQLGIEK	Calponin-homology (CH) 2 (exon 7)	
	Peptide hD3	LLDPEDVDTTYPDKK	Calponin-homology (CH) 2 (exon 7-8)	
	Peptide hD4	VGNILQLGSK	Spectrin Repeat 1 (exon 11)	
	Peptide hD5	TAALQSATPVER	Spectrin Repeat 16 (exon 43)	
	Peptide hD6	TDASILQEK	Spectrin Repeat 17 (exon 45)	
	Peptide hD7	QAEEVNTEWEK	Spectrin Repeat 23 (exon 59)	
	Peptide hD8	LNLHSADWQR	Spectrin Repeat 23 (exon 59)	
Dystrophin peptide sequences specific to large dystrophins (shared between WT dystrophin, midi-Dys, and full-Dys constructs)	Peptide L1	VLMDLQNQK	Spectrin Repeat 2 (exon 12)	**Figure 2D**
	Peptide L2	VLQEDLEQEQVR	Spectrin Repeat 2 (exon 13)	
	Peptide L3	QASEQLNSR	Spectrin Repeat 4 (exon 20)	
	Peptide L4	QTNLQWIK	Spectrin Repeat 18 (exon 47)	
	Peptide L5	DSTQWLEAK	Spectrin Repeat 21 (exon 53)	
	Peptide L6	DYSADDTR	Spectrin Repeat 21 (exon 54)	
	Peptide L7	SHLEASSDQWKR	Spectrin Repeat 22-23 (exon 57)	
	Peptide L8	ILADLEEENR	Carboxy-terminal domain (exon 74-75)	
	Peptide L9	DAELIAEAK	Carboxy-terminal domain (exon 75)	
	Peptide L10	QLESQLHR	Carboxy-terminal domain (exon 75)	
	Peptide L11	QLLEQPQAEAK	Carboxy-terminal domain (exon 75-76)	

Figure 1: Schematic representation of dystrophin clones tested, split intein approach to express large constructs and proteomics workflow. A) structural organization of full-length dystrophin (muscle isoform Dp427). µDys currently evaluated in clinical trials, and midi-dystrophin (ΔSR5-15). **B)** Dual vector strategy to express a midi-dystrophin using split intein gp41.1. **C)** Triple vector strategy to re-express full-length dystrophin using two orthogonal split inteins Nrdj1 and gp41.1. **D)** Workflow for characterization of the protein expression profile in *mdx*^{4cv} skeletal muscle. Gastrocnemius muscles were isolated from wild-type, saline-treated *mdx*^{4cv} or systemically injected *mdx*^{4cv} with low doses of AAVMYO1. Total proteins from six muscles per group were extracted and labeled with TMT isobaric tags before protein quantification using LC-MS/MS.

Figure 2: Detection of dystrophin expression and quantification of peptide-specific abundance using proteomics. Dystrophin peptide abundances were quantified using TMT proteomics in gastrocnemius muscle samples of WT, *mdx*^{4cv} treated with saline or AAVMYO1 to express µDys-*mdx*^{4cv}, midiDys-*mdx*^{4cv}, and full-Dys-*mdx*^{4cv}. **A**) Quantified abundance of AAV-mediated dystrophin expressed in *mdx*^{4cv} mice *versus* endogenous full-length dystrophin in WT mice. **B**) Abundance of peptides present only in full-length dystrophin (endogenous dystrophin in WT and full-Dys construct *via* triple AAVMYO1 treatment). **C**) Abundance of peptides specific to transgenic/human dystrophins (shared between µDys5, midi-Dys, and full-Dys constructs) delivered by AAVMYO1. **D**) Abundance of peptides specific to large dystrophins (endogenous WT dystrophin, or AAV-delivered midi-Dys and full-Dys constructs). The non-zero value for dystrophin peptides in saline-treated *mdx*^{4cv} is most likely due to co-isolation interference common to TMT proteomics analyses. Bar graphs depict mean ±SEM of n=6 mice/group, except peptide L7 and L10 were n=3. Comparisons between groups were made using one-way ANOVA with

Tukey's multiple comparisons test. $^{***}P<0.001$ *versus* WT; $^{\$\$\$}P<0.001$ *versus* *mdx*^{4cv} saline. µDys: micro-dystrophin, mDys and midi-Dys: midi-dystrophin, fDys and full-Dys: full-length dystrophin.

Figure 3: Histology analysis of gastrocnemius muscle cross-sections showing improvements with dystrophin constructs. A) representative images of gastrocnemius muscle cross-sections stained with H&E or Trichrome (Top rows, scale bars: 50µm), or immunolabeled with antibodies specific to periostin (scale bars: 50µm) or dystrophin-glycoproteins elements (lower panel, scale bars: 100µm). These images were taken in RGB colors but inverted to black and white for better visualization. The original panel is presented in the Supplementary Figure 2 and Supplementary Figure 3. **B)** Percentage of dystrophin-positive fibers. 600-1000 myofibers were counted per sample, with n=6 analyzed per group. **C)** The collagen area of the gastrocnemius muscle was measured using Trichrome-stained cross-sections. n=5 samples per group. **D)** Gastrocnemius myofiber area and **E)** minimal Feret's diameter. More than 700 myofibers per sample from n=6 per group were analyzed. The average values are shown on top of the violin bars. The solid line represents the median, while the dashed lines show the quartiles. **F)** Periostin area measured from cross-section muscle sections immunolabeled with specific antibodies against periostin. n=6 samples per group. **G)** Periostin abundance level detected from proteomics analysis of gastrocnemius muscles. **H)** Abundance levels of different collagens were measured using the proteomics method from gastrocnemius samples. NS: Not significant, $^{*}P<0.05$, $^{**}P<0.01$,$^{***}P<0.001$ *versus* WT; $^{\$}P<0.05$, $^{\$\$}P<0.01$, $^{\$\$\$}P<0.001$ *versus* saline group; $^{\#}P<0.05$, $^{\#\#}P<0.01$, $^{\#\#\#}P<0.001$ *versus* µDys group; $^{\&\&}P<0.01$ *versus* midi-Dys group using ANOVA test followed by Tukey's post hoc. Dys+: dystrophin-positive. H&E: Hematoxylin and Eosin staining.

863 μDys: micro-dystrophin, mDys and midi-Dys: midi-dystrophin, fDys and full-Dys: full-length
864 dystrophin.

865 **Figure 4: Comparison of protein expression profiles between experimental groups.** Protein
866 expression profiles in gastrocnemius muscle were compared between WT mice and **A)** saline-
867 *mdx*^{4cv}, **B)** *mdx*^{4cv} injected with single AAVMYO1 μDys, **C)** *mdx*^{4cv} injected with dual AAVMYO1
868 to express midi-dystrophin or **D)** *mdx*^{4cv} injected with triple AAVMYO1 vector to express full-
869 length dystrophin. A two-way unpaired Student's t-test was used to calculate *P*-values for pairwise
870 fold changes, and the Benjamini Hochberg method was used to control the false discovery rate
871 (FDR). Corrected *P*-values were log-transformed and plotted against log-transformed fold change
872 values to obtain volcano plots, and a minimum corrected *P*-value cutoff of 0.05 and minimum
873 relative fold change cutoff of ±1 were applied to identify differentially expressed proteins (DEPs)
874 in pairwise comparisons. Data were collected from a sample size of n=6 per group.

875 **Figure 5: Analysis of protein expression profile demonstrates proteomic rescue by dystrophin**
876 **constructs. A)** Heat map depicting the top upregulated and downregulated proteins between WT
877 and *mdx*^{4cv} muscle. Gene ontology (GO) enrichment analysis was performed using GOrilla and
878 g:Profiler to determine the molecular function (MF), biological process (BP), and cellular
879 compartment (CC) enrichment of significantly **B)** upregulated and **C)** downregulated proteins in
880 *mdx*^{4cv} gastrocnemius muscle compared to WT muscle.

881 **Figure 6: dystrophin delivery alleviates DGC protein defects in *mdx*^{4cv} mice:** Relative
882 abundance of **A)** sarcoglycans, **B)** dystroglycan, dystrobrevin, **C)** syntrophins, **D)** utrophin, and **E)**
883 protein-arginine deiminase type-2, myoglobin, and tubulin beta 6 class V measured by the
884 proteomics method. Bar graphs depict means ± SEM from n=5-6 mice/group. Comparisons

between groups were made using one-way ANOVA with Tukey's multiple comparisons test. NS: Not significant, $^{*}P<0.05$, $^{**}P<0.01$, $^{***}P<0.001$ *versus* WT; $^{\$}P<0.05$, $^{\$\$}P<0.01$, $^{\$\$\$}P<0.001$ *versus* saline group; $^{\#\#}P<0.01$, $^{\#\#\#}P<0.001$ *versus* µDys group; $^{\&}P<0.05$, $^{\&\&}P<0.01$ *versus* midi-Dys. µDys: micro-dystrophin, mDys: midi-dystrophin, fDys: full-length dystrophin.

Figure 7: Amelioration of altered membrane repair and myogenesis pathway markers in *mdx*^{4cv} muscle mediated by AAV-dystrophin constructs. A) Heat map showing elevated expression of various proteins implicated in membrane trafficking and repair in *mdx*^{4cv} gastrocnemius muscle and partial restoration with µDys5, midi-dystrophin, or full-length dystrophin delivered by AAV vectors. **B)** Annexin (A1, A4, and A5) abundance in WT, dystrophic, or AAV-treated muscles. **C)** Abundance of proteins involved in muscle repair. **D)** Expression of key proteins involved in membrane trafficking and remodeling. **E)** Galectin-1 and **F)** galectin-3 abundance in *mdx*^{4cv} and WT muscles. Bar graphs represent means ± SEM of n=6 mice/group. NS: Not significant, $^{*}P<0.05$, $^{**}P<0.01$, $^{***}P<0.001$ *versus* WT; $^{\$}P<0.05$, $^{\$\$}P<0.01$, $^{\$\$\$}P<0.001$ *versus* saline group using one-way ANOVA test followed by Tukey's post hoc. µDys: micro-dystrophin, mDys: midi-dystrophin, fDys: full-length dystrophin.

Figure 8: Proteins with unrestored expression in *mdx*^{4cv} mice treated with various dystrophin constructs. Heat maps displaying proteins that did not display significant restoration to WT levels in **A)** µDys5-*mdx*^{4cv}, **B)** midi-Dys-*mdx*^{4cv}, or **C)** full-Dys-*mdx*^{4cv} gastrocnemius muscles. Exemplary proteins with unrestored levels in AAV-Dys construct groups include **D)** carboxylesterase 1D (Ces1d), **E)** spermine oxidase (Smox), **F)** tRNA methyltransferase 10 homolog C (Trmt10c), **G)** adenosylmethionine decarboxylase (Amd1), **H)** histone H1.2 (H1-2), **I)** myosin light chain 6B (Myl6b), **J)** heme binding protein (Hebp1), **K)** nicotinamide nucleotide transhydrogenase (Nnt), and **L)** eukaryotic translation initiation factor 2D (Eif2d). Bar graphs

depict mean±SEM from n=5-6 mice/group. Comparisons between groups were made using one-way ANOVA with Tukey's multiple comparisons test. $^{*}P<0.05$, $^{**}P<0.01$, $^{***}P<0.001$ *versus* WT; $^{\$}P<0.05$, $^{\$\$\$}P<0.001$ *versus* saline. $^{\#}P<0.05$, $^{\#\#}P<0.01$ *versus* µDys group. µDys: micro-dystrophin, mDys: midi-dystrophin, fDys: full-length dystrophin.

Figure 1:

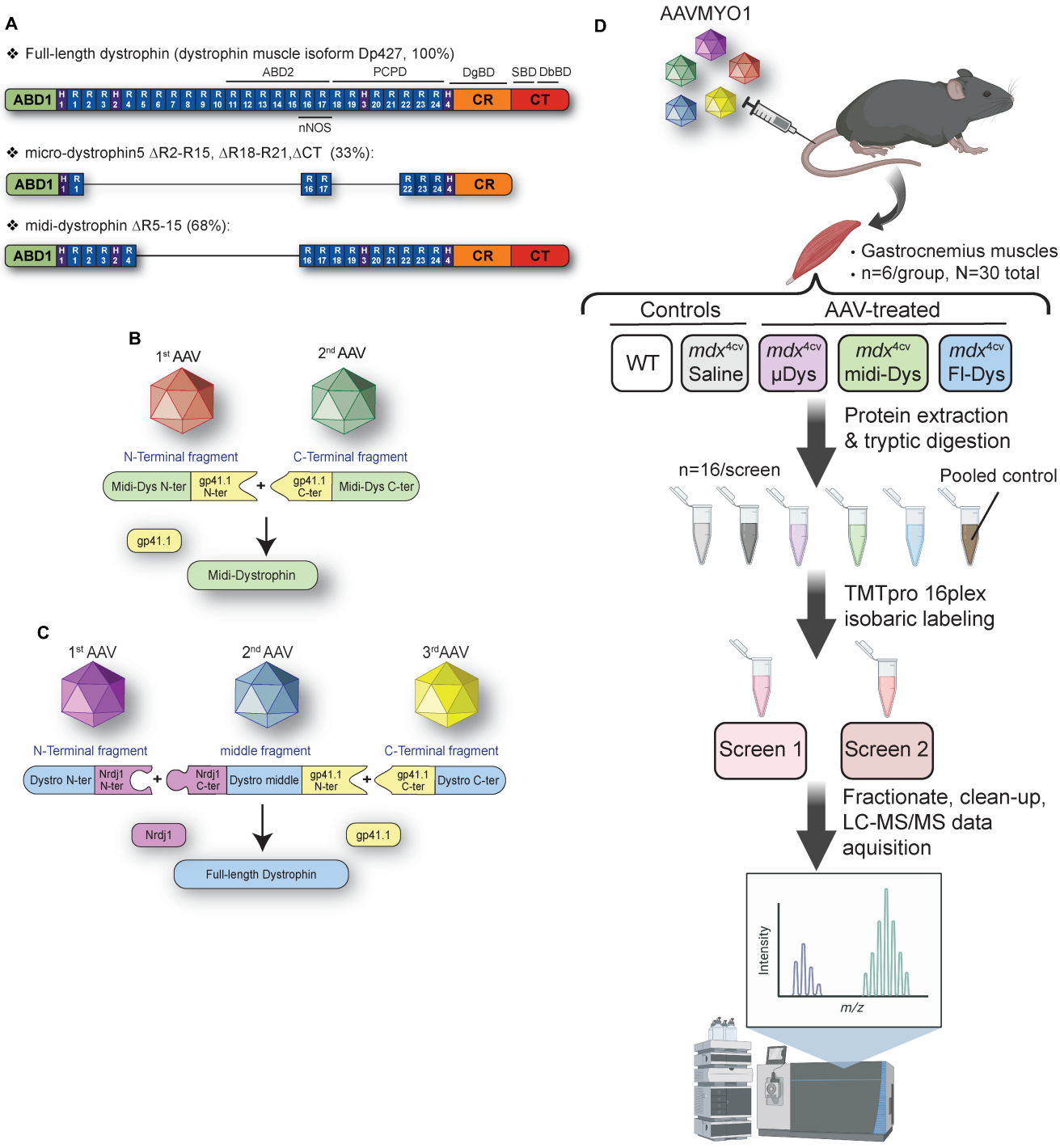
A
❖ Full-length dystrophin (dystrophin muscle isoform Dp427, 100%)
ABD2
PCPD
DgBD
SBD DbBD
ABD1
CR
CT
nNOS
❖ micro-dystrophin5 ΔR2-R15, ΔR18-R21,ΔCT (33%):
❖ midi-dystrophin ΔR5-15 (68%):
B
1st AAV
2nd AAV
N-Terminal fragment
C-Terminal fragment
Midi-Dys N-ter
gp41.1 N-ter
gp41.1 C-ter
Midi-Dys C-ter
gp41.1
Midi-Dystrophin
C
1st AAV
2nd AAV
3rdAAV
N-Terminal fragment
middle fragment
C-Terminal fragment
Dystro N-ter
Nrdj1 N-ter
Nrdj1 C-ter
Dystro middle
gp41.1 N-ter
gp41.1 C-ter
Dystro C-ter
Nrdj1
gp41.1
Full-length Dystrophin
D
AAVMYO1
• Gastrocnemius muscles
• n=6/group, N=30 total
Controls
AAV-treated
WT
mdx4cv Saline
mdx4cv µDys
mdx4cv midi-Dys
mdx4cv Fl-Dys
Protein extraction & tryptic digestion
n=16/screen
Pooled control
TMTpro 16plex isobaric labeling
Screen 1
Screen 2
Fractionate, clean-up, LC-MS/MS data aquisition
Intensity
m/z

Figure 2:

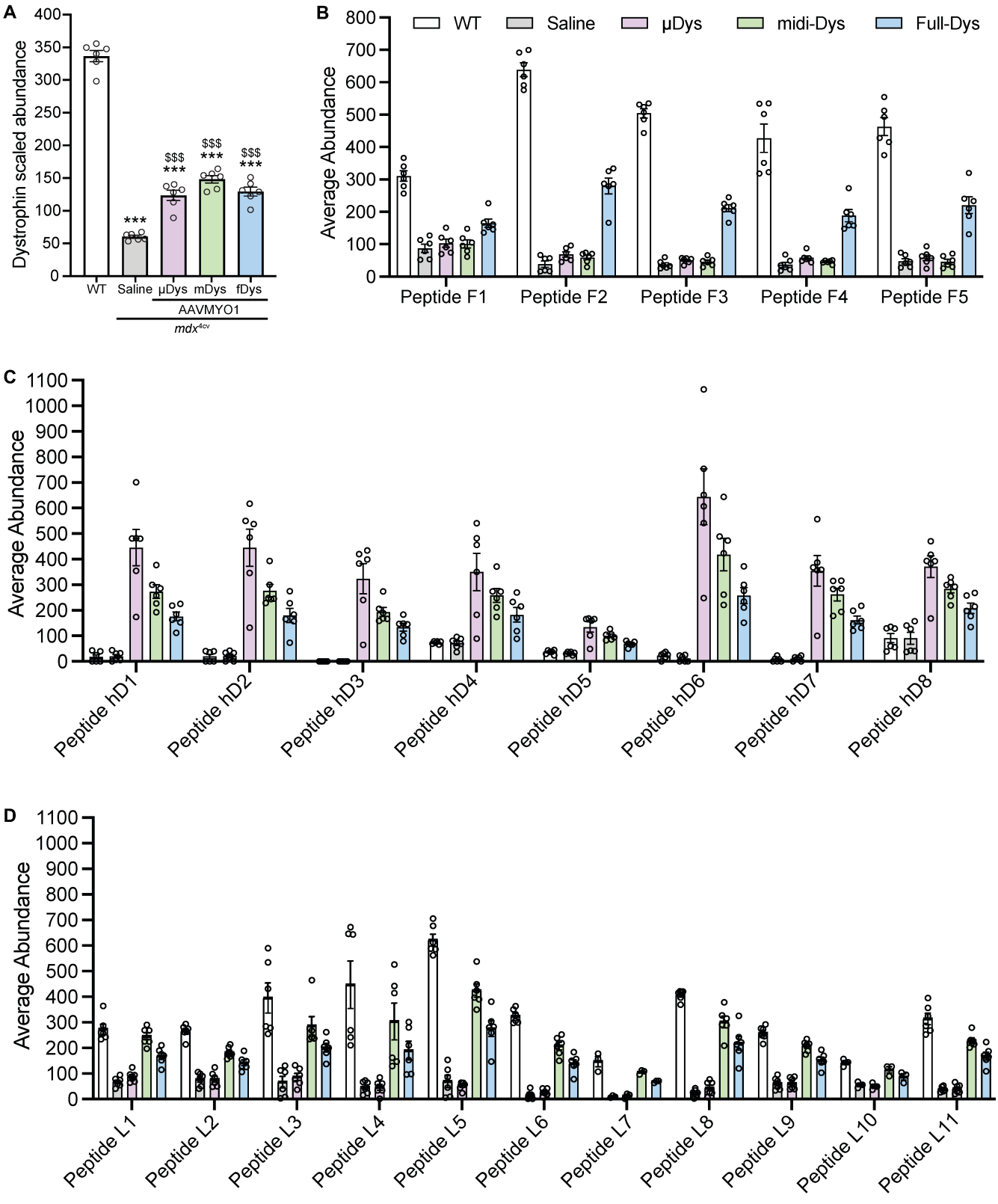
A
Dystrophin scaled abundance
WT
Saline
µDys
mDys
fDys
AAVMYO1
mdx4cv
B
WT
Saline
µDys
midi-Dys
Full-Dys
Average Abundance
Peptide F1
Peptide F2
Peptide F3
Peptide F4
Peptide F5
C
Average Abundance
Peptide hD1
Peptide hD2
Peptide hD3
Peptide hD4
Peptide hD5
Peptide hD6
Peptide hD7
Peptide hD8
D
Average Abundance
Peptide L1
Peptide L2
Peptide L3
Peptide L4
Peptide L5
Peptide L6
Peptide L7
Peptide L8
Peptide L9
Peptide L10
Peptide L11

Figure 3:

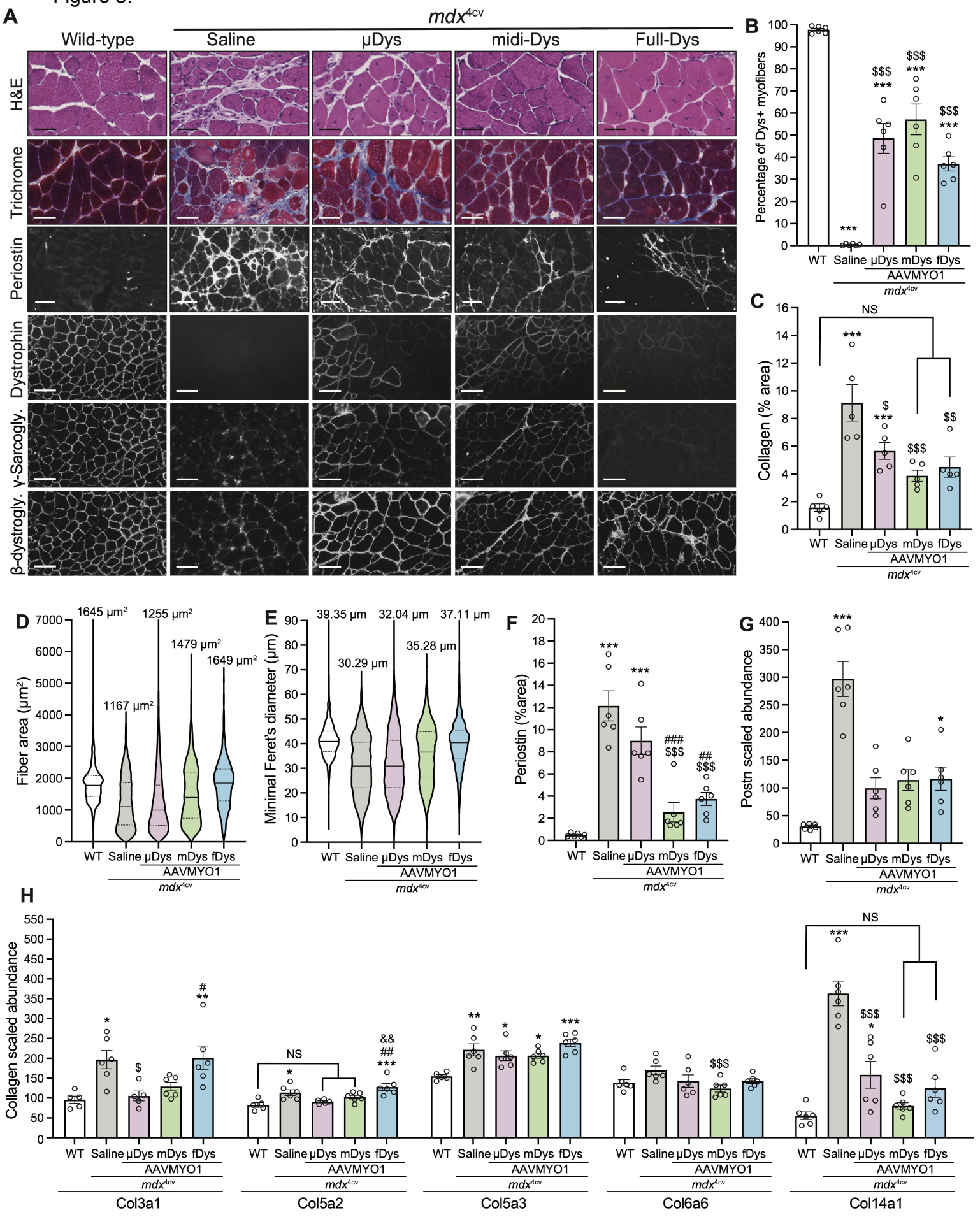
A
mdx4cv
Wild-type
Saline
µDys
midi-Dys
Full-Dys
H&E
Trichrome
Periostin
Dystrophin
γ-Sarcogly.
β-dystrogly.
B
Percentage of Dys+ myofibers
WT Saline µDys mDys fDys
AAVMYO1
mdx4cv
C
Collagen (% area)
NS
D
Fiber area (µm²)
1645 µm²
1255 µm²
1479 µm²
1649 µm²
1167 µm²
E
Minimal Feret's diameter (µm)
39.35 µm
32.04 µm
37.11 µm
30.29 µm
35.28 µm
F
Periostin (%area)
G
Postn scaled abundance
H
Collagen scaled abundance
Col3a1
Col5a2
Col5a3
Col6a6
Col14a1

Figure 4:

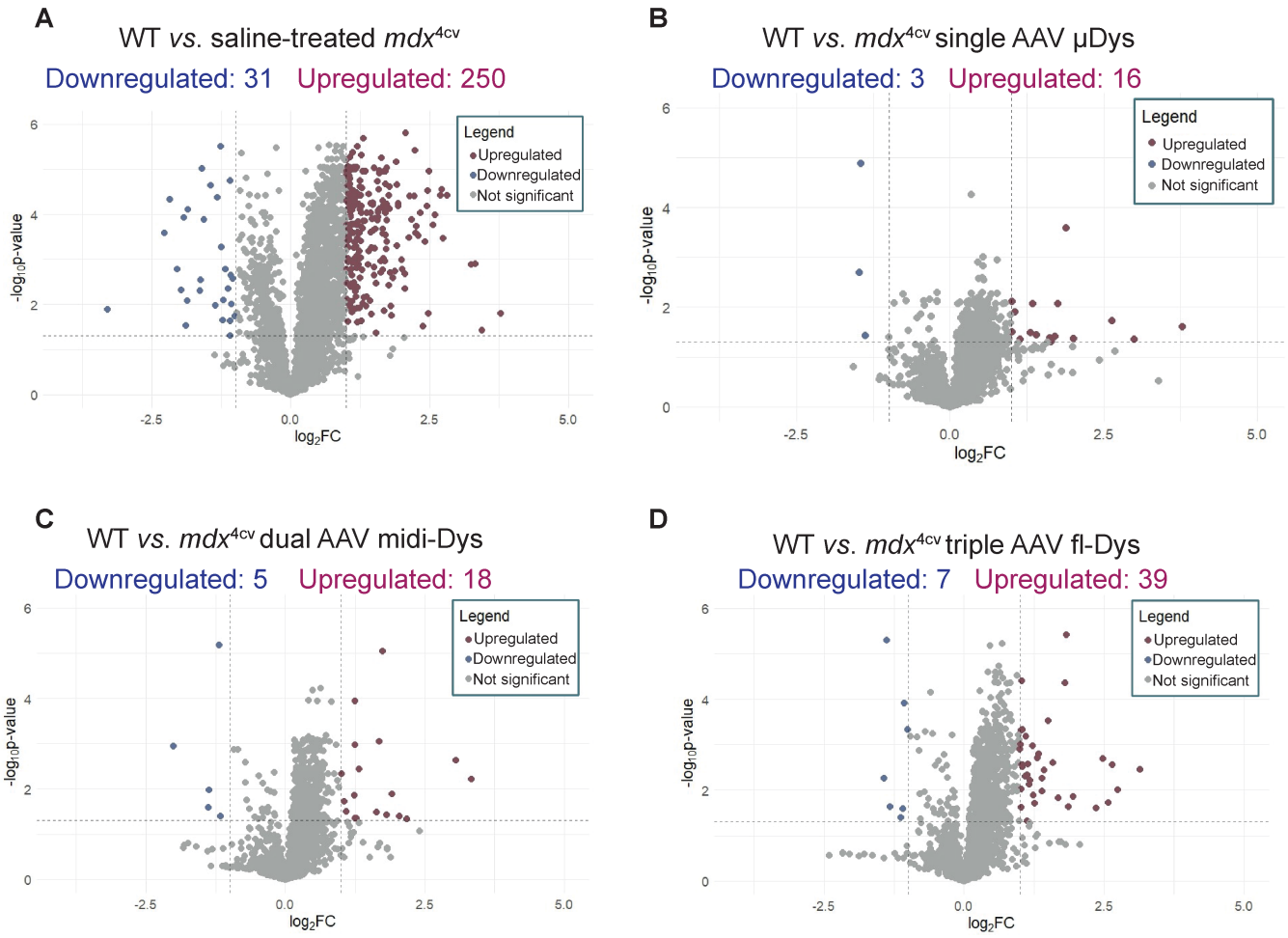
A
WT vs. saline-treated mdx4cv
Downregulated: 31
Upregulated: 250
B
WT vs. mdx4cv single AAV µDys
Downregulated: 3
Upregulated: 16
C
WT vs. mdx4cv dual AAV midi-Dys
Downregulated: 5
Upregulated: 18
D
WT vs. mdx4cv triple AAV fl-Dys
Downregulated: 7
Upregulated: 39
Legend
Upregulated
Downregulated
Not significant
-log10p-value
log2FC

Figure 5:

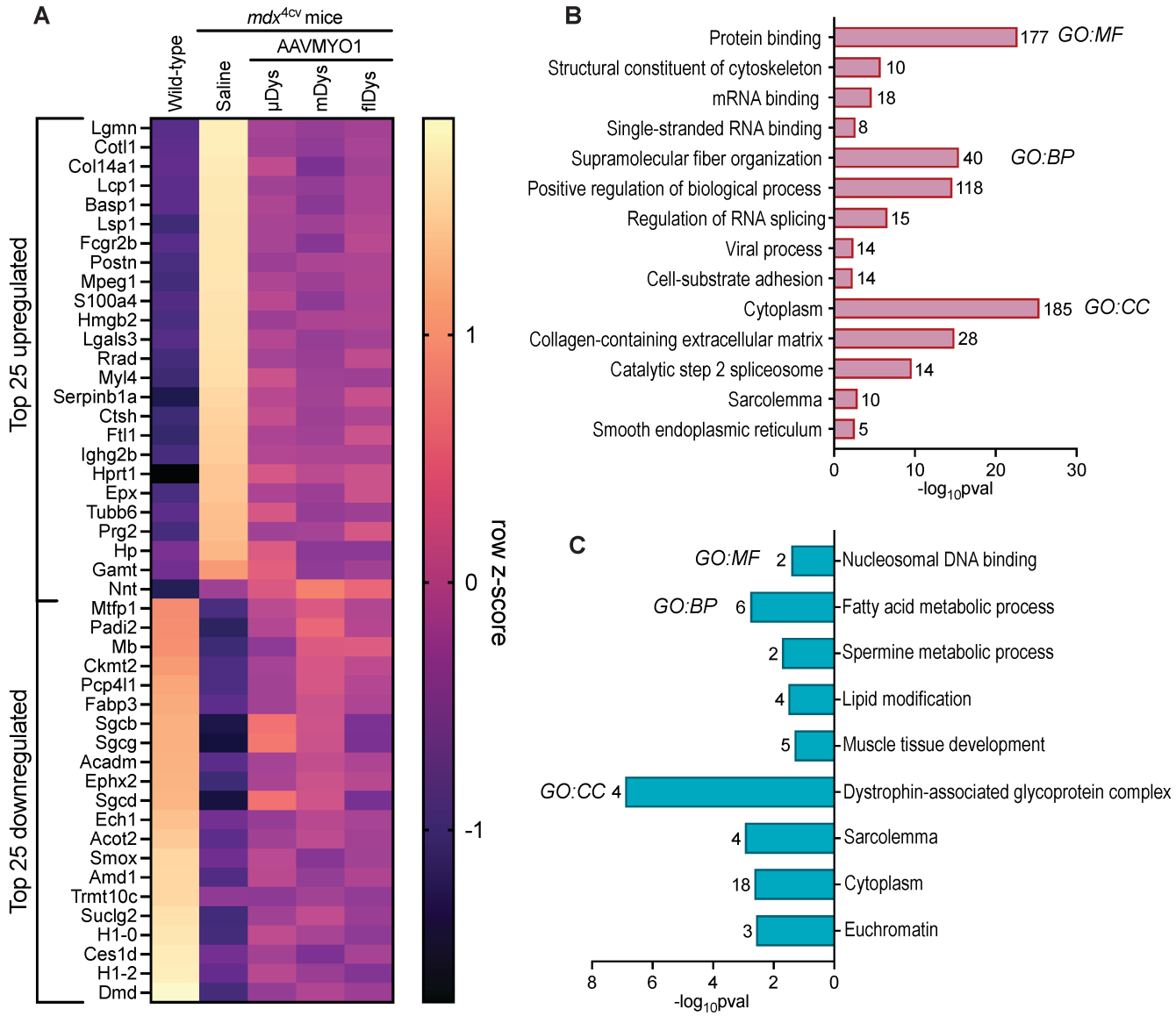
A
mdx4cv mice
AAVMYO1
Wild-type
Saline
µDys
mDys
fDys
Top 25 upregulated
Top 25 downregulated
Lgmn
Cotl1
Col14a1
Lcp1
Basp1
Lsp1
Fcgr2b
Postn
Mpeg1
S100a4
Hmgb2
Lgals3
Rrad
Myl4
Serpinb1a
Ctsh
Ftl1
Ighg2b
Hprt1
Epx
Tubb6
Prg2
Hp
Gamt
Nnt
Mtfp1
Padi2
Mb
Ckmt2
Pcp4l1
Fabp3
Sgcb
Sgcg
Acadm
Ephx2
Sgcd
Ech1
Acot2
Smox
Amd1
Trmt10c
Suclg2
H1-0
Ces1d
H1-2
Dmd
1
0
-1
row z-score
B
Protein binding 177 GO:MF
Structural constituent of cytoskeleton 10
mRNA binding 18
Single-stranded RNA binding 8
Supramolecular fiber organization 40 GO:BP
Positive regulation of biological process 118
Regulation of RNA splicing 15
Viral process 14
Cell-substrate adhesion 14
Cytoplasm 185 GO:CC
Collagen-containing extracellular matrix 28
Catalytic step 2 spliceosome 14
Sarcolemma 10
Smooth endoplasmic reticulum 5
0 10 20 30
-log10pval
C
GO:MF 2 Nucleosomal DNA binding
GO:BP 6 Fatty acid metabolic process
2 Spermine metabolic process
4 Lipid modification
5 Muscle tissue development
GO:CC 4 Dystrophin-associated glycoprotein complex
4 Sarcolemma
18 Cytoplasm
3 Euchromatin
8 6 4 2 0
-log10pval

Figure 6:

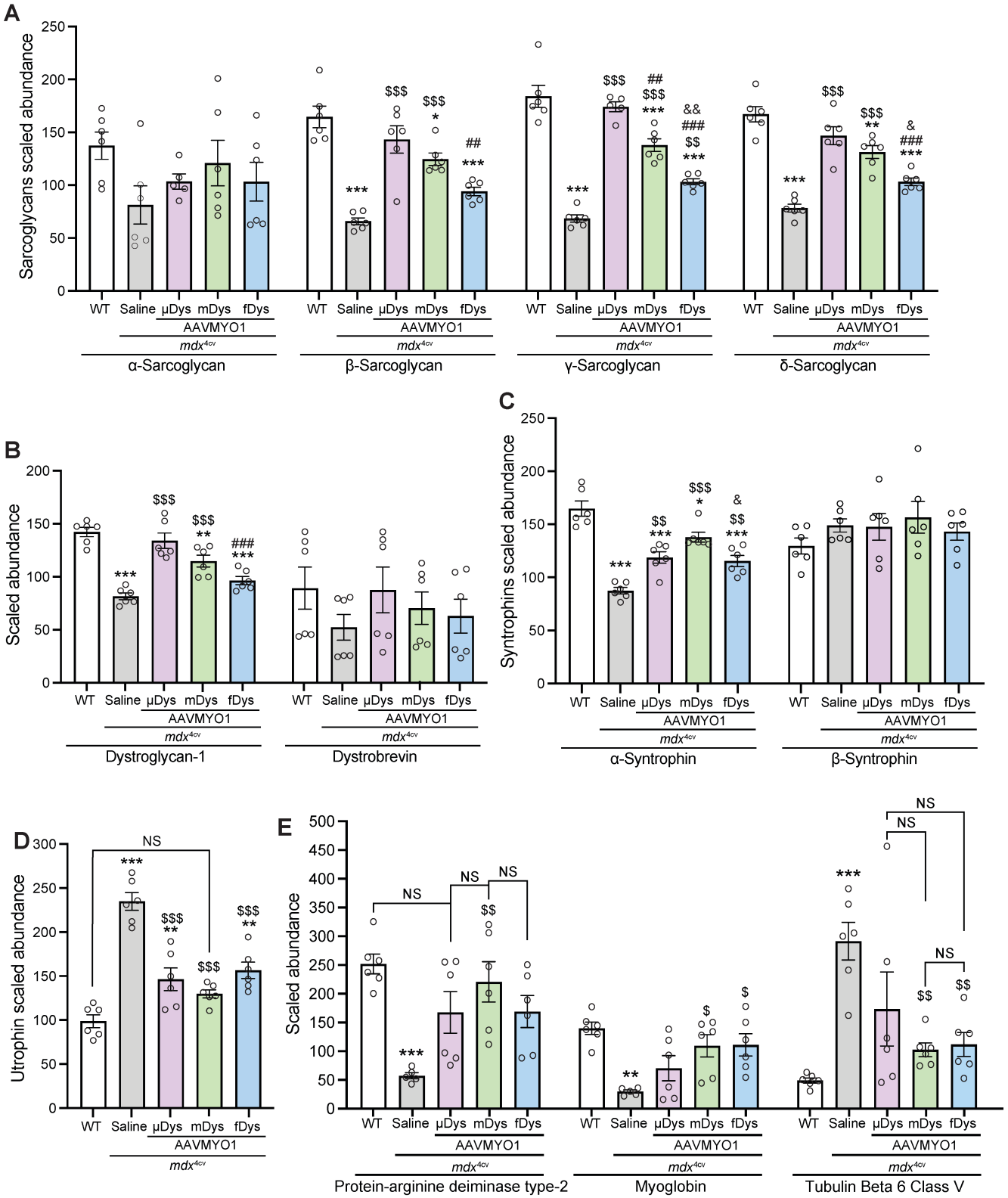
A
Sarcoglycans scaled abundance
WT
Saline
μDys
mDys
fDys
AAVMYO1
mdx4cv
α-Sarcoglycan
β-Sarcoglycan
γ-Sarcoglycan
δ-Sarcoglycan
B
Scaled abundance
Dystroglycan-1
Dystrobrevin
C
Syntrophins scaled abundance
α-Syntrophin
β-Syntrophin
D
Utrophin scaled abundance
NS
E
Scaled abundance
Protein-arginine deiminase type-2
Myoglobin
Tubulin Beta 6 Class V

Figure 7:

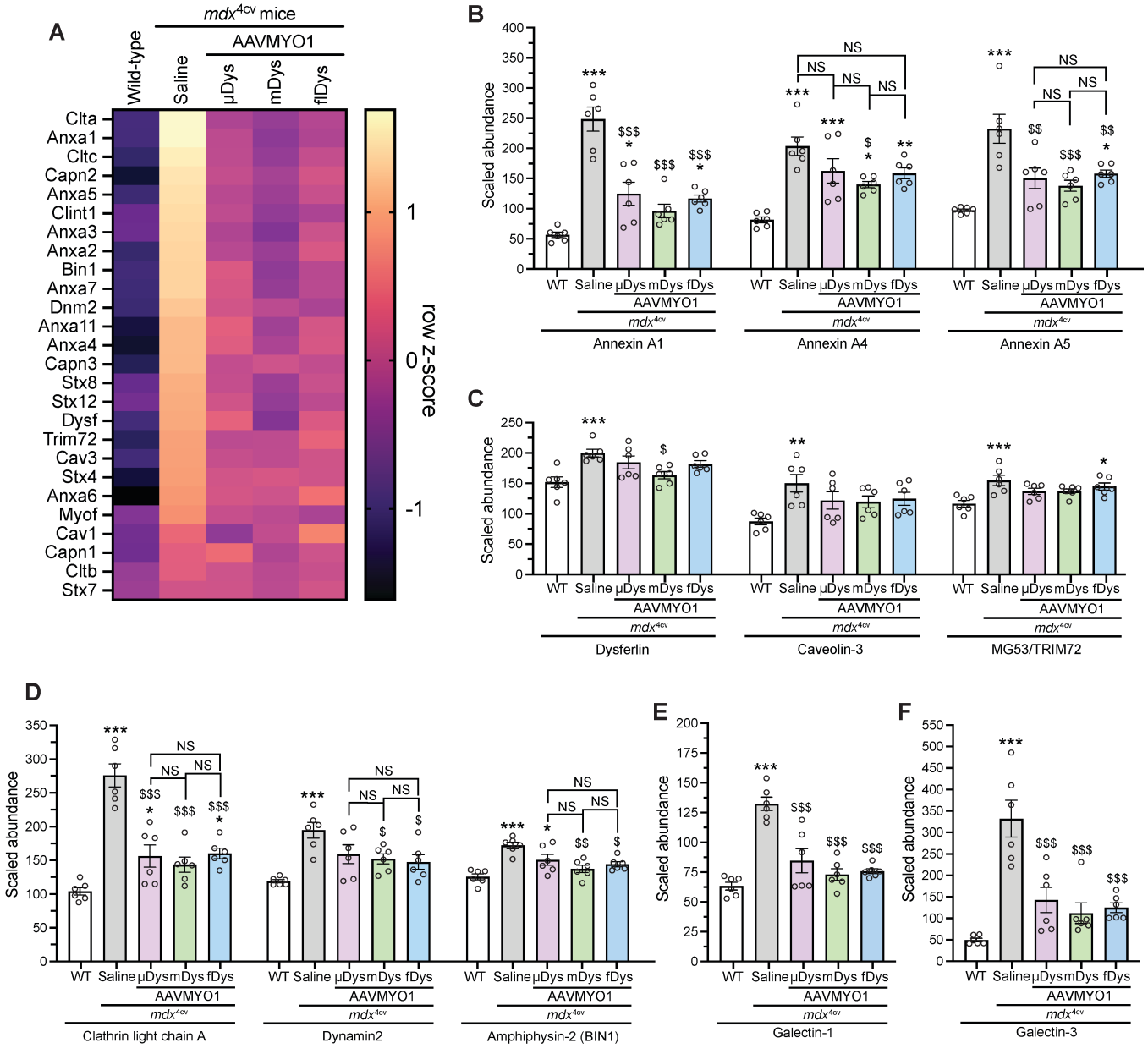
A
mdx4cv mice
AAVMYO1
Wild-type
Saline
µDys
mDys
fDys
Clta
Anxa1
Cltc
Capn2
Anxa5
Clint1
Anxa3
Anxa2
Bin1
Anxa7
Dnm2
Anxa11
Anxa4
Capn3
Stx8
Stx12
Dysf
Trim72
Cav3
Stx4
Anxa6
Myof
Cav1
Capn1
Cltb
Stx7
row z-score
1
0
-1
B
Scaled abundance
WT Saline µDys mDys fDys
AAVMYO1
mdx4cv
Annexin A1
Annexin A4
Annexin A5
C
Dysferlin
Caveolin-3
MG53/TRIM72
D
Clathrin light chain A
Dynamin2
Amphiphysin-2 (BIN1)
E
Galectin-1
F
Galectin-3
NS

Figure 8:

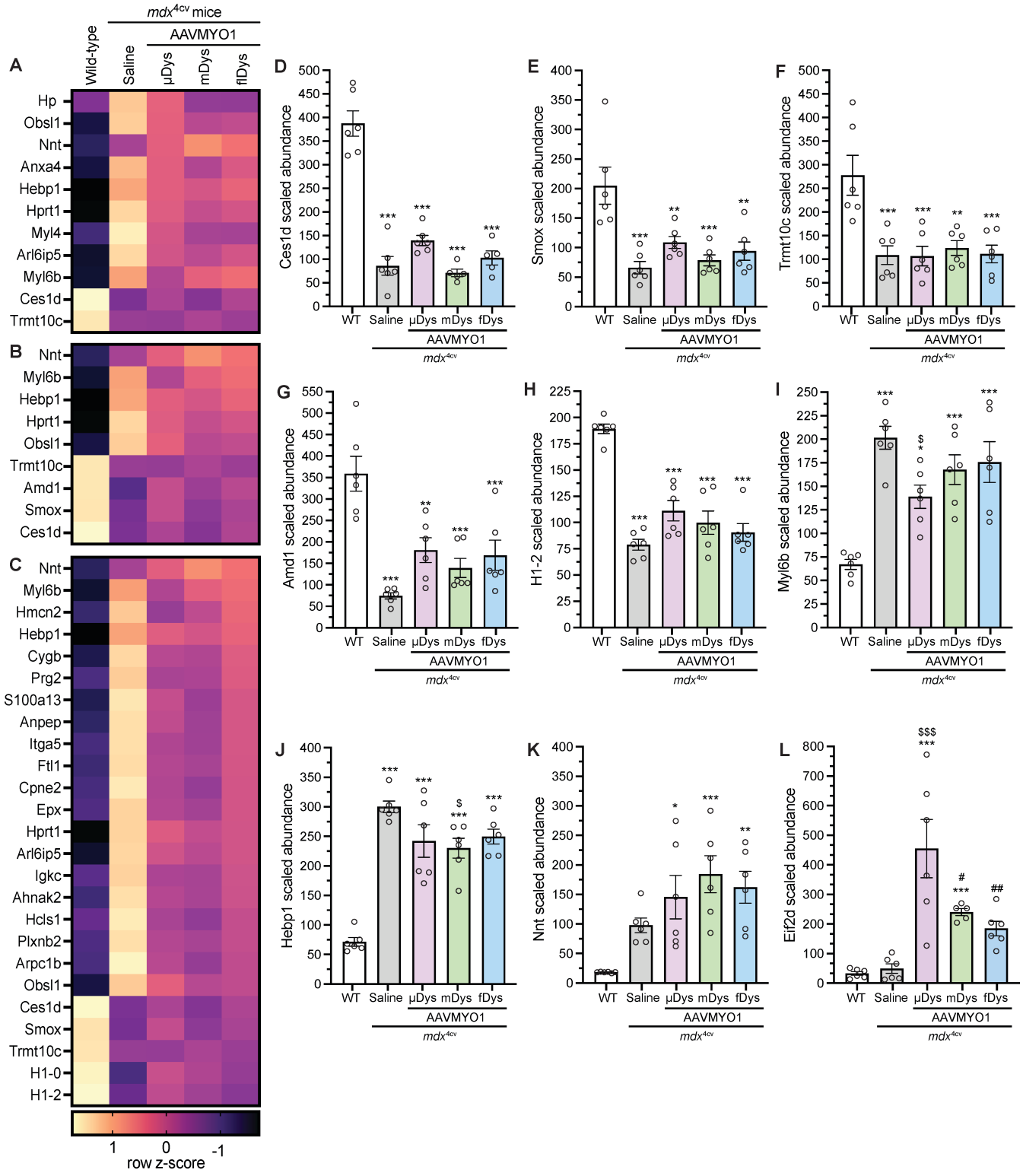
A
mdx4cv mice
Wild-type
Saline
AAVMYO1
µDys
mDys
fDys
Hp
Obsl1
Nnt
Anxa4
Hebp1
Hprt1
Myl4
Arl6ip5
Myl6b
Ces1d
Trmt10c
B
Nnt
Myl6b
Hebp1
Hprt1
Obsl1
Trmt10c
Amd1
Smox
Ces1d
C
Nnt
Myl6b
Hmcn2
Hebp1
Cygb
Prg2
S100a13
Anpep
Itga5
Ftl1
Cpne2
Epx
Hprt1
Arl6ip5
Igkc
Ahnak2
Hcls1
Plxnb2
Arpc1b
Obsl1
Ces1d
Smox
Trmt10c
H1-0
H1-2
1
0
-1
row z-score
D
Ces1d scaled abundance
E
Smox scaled abundance
F
Trmt10c scaled abundance
G
Amd1 scaled abundance
H
H1-2 scaled abundance
I
Myl6b scaled abundance
J
Hebp1 scaled abundance
K
Nnt scaled abundance
L
Eif2d scaled abundance
WT
Saline
µDys
mDys
fDys
AAVMYO1
mdx4cv